University of Regensburg Institute of Theoretical Physics

Electronic excitation spectra of metallic tip-substrate nanostructures from time-dependent density functional theory

Bachelor's thesis

by

Adil Gafarzada

September 25, 2025

Reviewer: Dr. Jan Wilhelm

Contents

Chapter 1

Introduction

Time-resolved nanoscopy has become a key route to watch electrons move on their characteristic spatial and temporal scales. Among the newest techniques, which also inspired this work, is near-field optical tunneling emission (NOTE) microscopy [1]. It pushes spatial resolution to the subnanometer scale and temporal resolution to the subcycle regime. A nutshell description of NOTE microscopy is given in Fig. 1.1.

What makes NOTE microscopy special is that the tunneling dynamics is driven and read out entirely optically, avoiding the limits of current measurements and the need for electrical contact, thus making the technique applicable to nonconducting materials [1]. Given this promise, focused theoretical efforts toward its description are worthwhile.

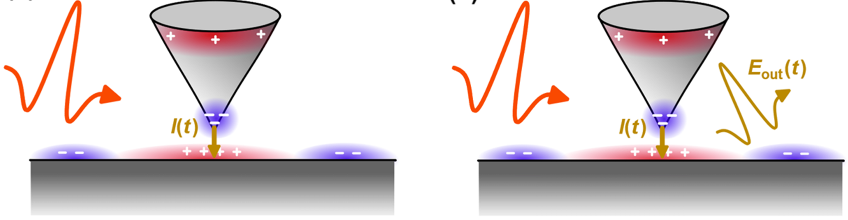

Figure 1.1: A typical experimental setup of NOTE microscopy: (a) A metallic tip and a metallic substrate are brought to a distance of a few Å and the system is illuminated by an ultrashort laser pulse. (b) The laser pulse induces electron dynamics and effectively polarizes the system. A strong near field emerges in the gap. (c) Electrons tunnel across the gap in synchrony with the driving laser pulse. (d) Accelerated charges emit radiation in the near field that is detected optically. Adapted from [1, 2].

The central question we take first steps toward in this work is: at which excitation energies is the tunneling dynamics most efficiently driven and can we identify these using theoretical tools alone, without having to conduct experiments?

We address this question by employing density functional theory (DFT) and its time-dependent extension, TDDFT. Briefly, a short, weak perturbation excites the system and by computing the time-dependent dipole moment from the time-dependent electron density, we acquire the excitation spectrum. Obtaining excitation spectra for compact metallic clusters has been demonstrated before in numerous works (for example, the work of Calvayrac [3]) with reasonable accuracy. In our work, while using a similar theoretical path, we focus on metallic tip–substrate structures and obtain the relevant excitation energies from the dipole oscillations of the cluster, which correspond to the energies absorbed by the system [4].

These findings are useful for both theory and experiment, as knowing which energies are absorbed while charge transitions across the gap can provide useful information for NOTE-like techniques and help to interpret the observations. The investigation brings several challenges, such as distinguishing gap modes from the dynamics inherent to the tip or substrate, tracking how the excitation spectrum responds to geometric variations (cluster size, gap distance) and providing robustness over dozens of calculations.

While solving the many-electron problem with pen and paper is not an option and solving the full Schrödinger equation for large systems is computationally infeasible, DFT offers an efficient alternative for static problems and TDDFT extends it to excitations and real-time dynamics. As the most important prerequisites for this work, we first introduce the essential concepts of DFT and TDDFT and demonstrate how to extract the excitation spectrum, and provide a theoretical framework within which the observations are interpretable. After establishing the workflow, we apply it to small metallic tip–substrate nanostructures, systematically vary the cluster size and gap distance and also justify the parameters used in our calculations. While coming short in quantitative extendability to large real-life experimental setups, the results delivered in this work are qualitatively valuable and consistent with state-of-the-art knowledge, opening up the path for future work to cover the quantitative part.

Chapter 2

Ground state density functional theory - theoretical foundations

This chapter introduces the theoretical foundations of the ground state density functional theory (DFT), which are indispensable for the subsequent time-dependent calculations. Having its roots in the 1920s, DFT became a complete and accurate theory in the 1960s with the publications of Kohn, Hohenberg and Sham [5].

We begin with the quantum mechanical many-body problem and the Born-Oppenheimer approximation, followed by the reformulation of the problem via the Hohenberg-Kohn theorems, which introduce the characteristic density functionals. Building on this basis, we present the Kohn-Sham construction, derive the Kohn-Sham equations together with their self-consistent solution and discuss some practical aspects of the calculations, such as basis sets and pseudopotentials. Finally, we give a brief overview of the most common exchange-correlation approximations.

The goal is to demonstrate why and how a density-based method circumvents the complexity of the complete many-body Schrödinger equation, without compromising on its predictive power and credibility.

This chapter closely follows standard treatments as presented in foundational texts by Ullrich [4], Parr and Yang [5] and Jensen [6]. The logical order and some of the physical formulations were inspired by the Lecture Notes of Jan Wilhelm [2].

2.1 The many-electron problem

We start with the time-independent, non-relativistic Schrödinger equation in its most general form

$$\hat{H}\Psi_n = E_n\Psi_n. \tag{2.1}$$

Here, $\hat{H}$ is the Hamiltonian, Ψ_n is the nth eigenfunction that solves the eigenvalue equation (2.1) with the corresponding energy eigenvalue E_n. The lowest energy eigenvalue is referred to as the *ground state energy* and can be expressed as

$$E = \min_n E_n, \tag{2.2}$$

with the corresponding eigenfunction Ψ denoted as the *ground state wave function.*

The wave function Ψ depends on the spatial coordinates of the electrons and the nuclei in the system

$$\Psi = \Psi(\mathbf{r}, \mathbf{R}), \tag{2.3}$$

where $\mathbf{r}$ and $\mathbf{R}$ denote the ordered sets of all coordinates in a system with N electrons and K nuclei respectively, in the following notation [2]:

$\mathbf{r}_i = (x_i, y_i, z_i)$	Coordinate vector of electron i, $\quad i = 1, \ldots, N$
$\mathbf{r} = (\mathbf{r}_1, \mathbf{r}_2, \ldots, \mathbf{r}_N)$	Ordered set of all electron coordinates
$\mathbf{R}_A = (x_A, y_A, z_A)$	Coordinates of atomic nuclei A, $\quad A = 1, \ldots, K$
$\mathbf{R} = (\mathbf{R}_1, \ldots, \mathbf{R}_K)$	Ordered set of all nuclear coordinates

Besides the kinetic energy operators of the nuclei, $\hat{T}_{nucl}$, and the electrons, $\hat{T}_e$, the total many-body Hamiltonian contains nucleus-electron, electron-electron and nucleus-nucleus interaction terms [2]

$$\hat{H}(\mathbf{r}, \mathbf{R}) = \hat{T}_{nucl}(\mathbf{R}) + \hat{T}_e(\mathbf{r}) + \hat{V}_{Ne}(\mathbf{r}, \mathbf{R}) + \hat{V}_{ee}(\mathbf{r}) + \hat{V}_{NN}(\mathbf{R}). \tag{2.4}$$

The kinetic energy operator of the electrons is

$$\hat{T}_e(\mathbf{r}) = -\frac{\hbar^2}{2m} \sum_i \nabla^2_{\mathbf{r}_i} \tag{2.5}$$

and for the nuclei

$$\hat{T}_{\text{nucl}}(\mathbf{R}) = -\sum_A \frac{\hbar^2}{2M_A} \nabla^2_{\mathbf{R}_A}. \tag{2.6}$$

The Coulomb potential energy terms are

$$\hat{V}_{Ne}(\mathbf{r}, \mathbf{R}) = -\sum_A \sum_i \frac{Z_A e^2}{|\mathbf{r}_i - \mathbf{R}_A|}, \tag{2.7}$$

$$\hat{V}_{ee}(\mathbf{r}) = +\sum_i \sum_{j>i} \frac{e^2}{|\mathbf{r}_i - \mathbf{r}_j|}, \tag{2.8}$$

$$\hat{V}_{NN}(\mathbf{R}) = +\sum_A \sum_{B>A} \frac{Z_A Z_B e^2}{|\mathbf{R}_A - \mathbf{R}_B|}. \tag{2.9}$$

Here, Z is the atomic charge of the nucleus, A and i are the running indices for the nuclei and the electrons, respectively. The inner sums in Eqs. (2.8) and (2.9) serve the purpose of avoiding double counting of the electrostatic interactions.

Relativistic kinetic energy corrections, spin-orbit, orbit-orbit, spin-spin coupling effects, as well as interactions with external electromagnetic fields are not covered by the Hamiltonian (2.4).

Born–Oppenheimer approximation

A crucial simplification of this Hamiltonian (2.4) is the Born-Oppenheimer approximation. The central idea is that the atomic nuclei are significantly heavier (a proton is about 1836 times heavier than an electron) and therefore move much more slowly. As a result, the nuclei are assumed to be fixed.

Under this assumption, electrons then adjust very fast to the nuclear motion. The two sets of degrees of freedom are then separated and the wave function $\Psi(\mathbf{r},\mathbf{R})$ is then factorized into a nuclear part Ψ_{nucl} and an electronic part Ψ_e

$$\Psi(\mathbf{r},\mathbf{R}) = \Psi_{nucl}(\mathbf{R})\Psi_{e,\mathbf{R}}(\mathbf{r}). \tag{2.10}$$

Here, the wave function $\Psi_{e,\mathbf{R}}(\mathbf{r})$ depends parametrically on the nuclear positions $\mathbf{R}$, meaning the nuclear positions have to be provided as numbers. The nuclei-nuclei potential operator $\hat{V}_{NN}(\mathbf{R})$ enters the Schrödinger equation as a fixed parameter $V_{NN,\mathbf{R}}$ for each nuclear configuration and the kinetic energy of the nuclei $\hat{T}_{nucl}(\mathbf{R})$ gets "eliminated", yielding the modification of the Hamiltonian (2.4) for the many-electron system

$$\hat{H}_{e,\mathbf{R}}(\mathbf{r}) = \hat{T}_e(\mathbf{r}) + \hat{V}_{Ne,\mathbf{R}}(\mathbf{r}) + \hat{V}_{ee}(\mathbf{r}) + V_{NN,\mathbf{R}} \tag{2.11}$$

and the electronic Schrödinger equation becomes

$$\hat{H}_{e,\mathbf{R}}(\mathbf{r})\Psi_{e,\mathbf{R}}(\mathbf{r}) = E\Psi_{e,\mathbf{R}}(\mathbf{r}). \tag{2.12}$$

For simplicity, we drop the indices in the Eqs. (2.11) and (2.12)

$$\hat{H}(\mathbf{r})\Psi(\mathbf{r}) = E\Psi(\mathbf{r}). \tag{2.13}$$

This approximation reduces the many-body problem to calculating the electronic structure for fixed nuclear positions — forming the starting point for many electronic structure methods, including density functional theory. We are particularly interested in the ground state solution of the electronic Schrödinger equation (2.13). The reason is that, in typical solids and molecules, the lowest excited states are on the order of several electronvolts above the ground state and since we investigate the systems in moderate temperatures, their corresponding thermal energies are far too small to populate the higher excited states to any appreciable extent [2]. We will later see that in the context of time-dependent calculations, such as those presented in this work, the system is also initially prepared in its ground state and subsequently driven out of equilibrium by an external perturbation [4].

2.2 Ground state DFT

Solving the Schrödinger equation gives us full access to all quantum state information. For instance, by knowing the ground state eigenfunction Ψ_0, we now can estimate the value of any associated physical observable $\hat{O}$ by calculating the expectation value in the ground state

$$\hat{O}_0 = \langle \Psi_0 | \hat{O} | \Psi_0 \rangle. \tag{2.14}$$

Except for the special cases, such as for two-electron systems, systems with high symmetry and in reduced dimensionality, solving the full many-electron Schrödinger equation (2.13) is a huge challenge because of its overly complex numerical nature. The computational cost of it grows exponentially to astronomical numbers the bigger the N gets [2]. Several schemes were developed dedicated to cleverly finding approximate solutions, among which Hartree-Fock and quantum Monte Carlo approaches are notable examples [4].

But is it in practice even absolutely necessary to solve the many-body equation fully or are there other ways of obtaining the desired observable value, without having to face a huge exponentially growing computational challenge? After all, the exact wave function contains much more information that wouldn't concern us in practice. This is where DFT comes in consideration. It relieves us from the challenge of solving for the full Ψ and makes it possible to calculate **all properties** of a given many-body system from the density of electrons $n(\mathbf{r})$ [4].

2.2.1 Hohenberg-Kohn theorems

The so-called Hohenberg-Kohn theorems provide proofs to the bold claim that it is possible to determine all quantum properties from the density of electrons and how an electron density dependent energy functional can give us the ground state energy [7].

The density of electrons $n(\mathbf{r})$ is defined as the expectation value of the electron density operator $\hat{n}(\mathbf{r})$

$$n(\mathbf{r}) = \langle \Psi | \hat{n}(\mathbf{r}) | \Psi \rangle, \tag{2.15}$$

with Ψ being the many-electron wave function. The electron density operator $\hat{n}(\mathbf{r})$ is defined as

$$\hat{n}(\mathbf{r}) = \sum_{i=1}^{N} \delta(\mathbf{r} - \mathbf{r_i}), \tag{2.16}$$

with $\mathbf{r}_i$ being the coordinate of the electron i. If Ψ_0 is a ground state wave function, the corresponding $n_0(\mathbf{r})$ is then called the ground state electron density. Normalized, the electron density $n(\mathbf{r})$ gives the number of the electrons in the system [2]

$$\int n(\mathbf{r}) d^3 r = N. \tag{2.17}$$

The electronic Hamiltonian (2.11) is assumed to have the form

$$\hat{H}(\mathbf{r}) = \hat{T}(\mathbf{r}) + \hat{V}_{ext}(\mathbf{r}) + \hat{V}_{ee}(\mathbf{r}), \tag{2.18}$$

with an external potential

$$\hat{V}_{\text{ext}}(\mathbf{r}) = \int d^3 r \, v_{\text{ext}}(\mathbf{r}) \hat{n}(\mathbf{r}) \overset{(2.16)}{=} \sum_{i=1}^{N} v_{\text{ext}}(\mathbf{r}_i), \tag{2.19}$$

which is given by the sum over all N electrons of the potential v_{ext} arising from the interaction of each electron with all nuclei [4].

The kinetic energy $\hat{T}(\mathbf{r})$ and the electron-electron interaction potential $\hat{V}_{ee}(\mathbf{r})$ are given by the Eqs. (2.5) and (2.8).

Here, we dropped the electrostatic repulsion term $V_{NN}(\mathbf{R})$, because it is a constant, not an operator.

First Hohenberg–Kohn theorem

The external potential $v_{ext}(\mathbf{r})$ *is determined uniquely by the ground state electron density* $n_0(\mathbf{r})$*, up to a trivial additive constant* [8].

In this context, the term "uniquely" implies a bijective mapping between $n(\mathbf{r})$ and $v_{\text{ext}}(\mathbf{r})$, up to a constant shift. This means that from a given ground state electron density n_0 one can trace back to a single external potential $v_{\text{ext}}(\mathbf{r})$, which in turn reproduces the same density n_0 [2]

$$v_{ext}(\mathbf{r}) \leftrightarrow n_0(\mathbf{r}). \tag{2.20}$$

As we can determine the $v_{ext}(\mathbf{r})$ from the electron density, therefore the Hamiltonian (2.18) is uniquely determined as well. Since the Hamiltonian is determined (except for a constant shift of the energy), plugging it into the Schrödinger equation yields the many-body wave functions for **all** states Ψ_n with their corresponding energy E_n. The corollary to this theorem states that *all properties of the system can be determined given only the ground state density* n_0 [9].

The first Hohenberg-Kohn theorem establishes that all properties of a system can be reconstructed from its ground state density. But it does not provide us assurance that the trial density is in fact the ground state density. The second Hohenberg-Kohn Theorem gives a formal solution to this problem by introducing a functional $F[n]$, which delivers the ground state energy if the input (the electron density) is right [7].

Second Hohenberg–Kohn theorem: the variation principle

A functional of electron densities for the total energy $E[n]$ is defined as

$$E[n] = F[n] + \int v_{ext}(\mathbf{r})n(\mathbf{r})d^3r, \tag{2.21}$$

where $F[n]$ is a universal functional of electron density and valid for any number of particles N and *any* external potential. The ground state density n_0 is then obtained by minimizing $E[n]$, meaning the correct (ground state) density input provides the lowest (ground state) total energy E_0 [8]

$$E_0 = \min_{n \in L_N} E[n]. \tag{2.22}$$

Here, L_N is a function space of all electron densities of an N-electron system [2]

$$L_N = \left\{ \tilde{n} : \mathbb{R}^3 \to \mathbb{R} \;\middle|\; \int_{\mathbb{R}^3} \tilde{n}(\mathbf{r})\, d^3\mathbf{r} = N,\; \tilde{n}(\mathbf{r}) \geq 0\; \forall\, \mathbf{r} \in \mathbb{R}^3 \right\}. \tag{2.23}$$

For any external potential v_{ext}, the exact ground state energy is the global minimum of the energy functional (2.21), in other words, the value of this functional at the ground state density n_0 [9].

Let us now take the newly introduced functional $F[n]$ into the scope [2]

$$F[n] = T[n] + E_H[n] + E_{\mathrm{xc}}[n]. \tag{2.24}$$

It is independent of the external potential and includes three contributions:

- The kinetic energy functional $T[n]$ of electrons;
- the Hartree energy

  $$E_H[n] = \frac{1}{2} \int d^3r \int d^3r' \, \frac{n(\mathbf{r})\, n(\mathbf{r}')}{|\mathbf{r} - \mathbf{r}'|}, \tag{2.25}$$

  which is the classical Coulomb energy [4];
- the remaining part is called the exchange-correlation energy $E_{xc}[n]$. It is the non-classical contribution of all the electron-electron interactions other than Hartree energy. It is defined as $E_{xc}[n_0] = \langle \Psi_0 | \hat{V}_{ee} | \Psi_0 \rangle - E_H[n_0]$ for the ground state density n_0 and the ground state wave function Ψ_0. The exact form of this functional is also unknown and has to be approximated (see section 2.2.5).

The exact form of $F[n]$, once determined, enables us by minimizing the total Energy $E[n]$ to find the ground state with given v_{ext} [9]. The problem is that the exact form of $T[n]$ is unknown and in practice it is only approximated. The simplest approximation for the kinetic energy, Thomas-Fermi approximation, provides a simple local expression for the kinetic energy, but it fails to reproduce atomic shell structure and molecular binding [4]. This shortcoming is overcome by the Kohn–Sham formulation of DFT.

2.2.2 Kohn–Sham DFT

This section is based on the books of Ullrich [4] and Parr and Yang [5]. Kohn-Sham method is today crucial for most applications of DFT. The key insight here is to utilize single-particle orbitals and take advantage of an effective single-particle picture. In this formulation, the complicated interacting many-body system is replaced by a non-interacting reference system by introducing the so-called Kohn-Sham orbitals (KS orbitals) ψ_i. The electron density is obtained by summing the squared magnitudes of these single-particle functions

$$n(\mathbf{r}) = \sum_{i=1}^{N} |\psi_i(\mathbf{r})|^2, \tag{2.26}$$

under the orthonormality constraint, so that the reference system can be defined meaningfully

$$\langle\psi_i|\psi_j\rangle = \int d^3r \psi_i^*(\mathbf{r})\psi_j(\mathbf{r}) = \delta_{ij}. \tag{2.27}$$

At first glance, we see that the condition (2.26) can be fulfilled by many different combinations. In a certain way, efficiency is traded for accuracy, compared to the orbital-free formulation. This detour is, however, has been proven to be extraordinarily accurate in approximating the kinetic energy

$$T_s(\psi_1, \psi_2, \ldots, \psi_N) = \sum_{i=1}^{N} -\frac{\hbar^2}{2m}\langle\psi_i|\nabla^2|\psi_i\rangle, \tag{2.28}$$

where the scalar product is given as an integral

$$\langle\psi_i|\nabla^2|\psi_i\rangle = \int d^3r\, \psi_i^*(\mathbf{r})\nabla^2\psi_i(\mathbf{r}). \tag{2.29}$$

The remaining difference between $T[n]$ and $T_s[n]$ is presumably small and is absorbed into the exchange-correlation functional E_{xc}. The universal functional $F[n]$ is rewritten as

$$F[n] = T_s[n] + E_H[n] + E_{xc}[n], \tag{2.30}$$

whereas the $T_s[n]$ is directly accessible through KS orbitals, the Hartree energy $E_H[n]$ is the classical Coulomb interaction of electrons and the exchange-correlation functional E_{xc}

contains all remaining quantum mechanical effects beyond Hartree energy and the small correction to the kinetic part. Inserting it into the energy functional yields

$$E[n] \approx T_s[\psi_1, \psi_2, ..., \psi_N] + E_H[n] + E_{xc}[n] + E_{ext}[n], \tag{2.31}$$

where the density n is generated from the KS orbitals $\psi_1, \psi_2, ..., \psi_N$ as in (2.26). Note that the symbol $\approx$ in (2.31) indicates that (2.28) is only an approximation to the kinetic energy. It is central to Kohn-Sham DFT formulation that $\approx$ can also be written as $=$ and since the KS orbitals are chosen as such, that it is possible to write the $T_s[\psi_1, \psi_2, ..., \psi_N]$ as a functional of density $T_s[n]$. A detailed justification of these two statements is beyond the scope of this section and can be found in the literature [5]. Since we packed the kinetic energy correction to the exchange-correlation functional, it is also necessary to redefine this for Kohn-Sham DFT

$$E_{xc}^{KS}[n] = E_{xc}[n] + T[n] - T_s[n] \tag{2.32}$$

and the total energy functional becomes

$$E[n] = T_s[n] + E_H[n] + E_{xc}^{KS} + E_{ext}[n], \tag{2.33}$$

with the external energy defined as

$$E_{ext}[n] := \int d^3r \, v_{ext}(\mathbf{r}) n(\mathbf{r}). \tag{2.34}$$

An important point is that accounting for the difference between E_{xc}^{KS} and E_{xc} in treatment of the exchange-correlation energy is still not exact in practical applications and remains a major challenge to this day. We will see in a later section how the exchange-correlation functional can be approximated, that in the end one can use it to accurately minimize the energy

$$E_0 = \min_{n(\mathbf{r})} \; E[n] = \min_{n(\mathbf{r})} \; \left[T_s[n] + E_H[n] + E_{xc}^{KS} + E_{ext}[n]\right], \tag{2.35}$$

to compute the ground state energy E_0.

2.2.3 Kohn-Sham equations

The minimizing process of the energy functional (2.35) in practical calculations is not carried out directly over the electron density, but over the KS orbitals, which generate the density via (2.26) considering the orthonormality constraint. We use the Lagrange multiplier method

$$L = T(\psi_1, \psi_2, \ldots, \psi_N) + E_H[n] + E_{xc}[n] + E_{ext}[n] - \sum_{n=1}^{N} \sum_{m=1}^{N} \lambda_{nm} \left(\langle \psi_n | \psi_m \rangle - \delta_{nm}\right) \tag{2.36}$$

and by minimizing the Lagrange function with respect to $\psi_1, \psi_2, ..., \psi_n$ one obtains the **Kohn-Sham equations** [2, 6]

$$\left[-\frac{\hbar^2}{2m}\nabla^2 + v_H(\mathbf{r}) + v_{xc}(\mathbf{r}) + v_{ext}(\mathbf{r})\right]\psi_n(\mathbf{r}) = \varepsilon_n \psi_n(\mathbf{r}), \tag{2.37}$$

with

- the parameters ε_n - the so-called Kohn-Sham eigenvalues, arising as the Lagrange multipliers $\varepsilon_n = \lambda_{nn}$. Although they do not represent the exact single-particle energies, they acquire physical significance in connection with ionization properties [10].

- Hartree potential

$$v_H(\mathbf{r}) = e^2 \int d^3r' \, \frac{\sum_{i=1}^{N} |\psi_i(\mathbf{r}')|^2}{|\mathbf{r} - \mathbf{r}'|}; \tag{2.38}$$

- the exchange correlation potential, which is formally calculated as a functional derivative of the exchange correlation energy

$$v_{xc}(\mathbf{r}) = \frac{\delta E_{\mathrm{xc}}[n]}{\delta n(\mathbf{r})}; \tag{2.39}$$

- and the external potential

$$v_{ext}(\mathbf{r}) = -\sum_A \frac{Z_A e^2}{|\mathbf{r} - \mathbf{R}_A|} \tag{2.40}$$

  represents the Coulomb potential of ion cores.

Self-consistency of Kohn-Sham equations

In practical algorithms the Kohn-Sham equations are treated iteratively in a so-called self-consistent field (SCF) procedure, which can be outlined as follows:

1. We start from an initial guess of the electron density, which is then used to construct the effective potential $v_{eff}(\mathbf{r})$ (sum of v_{xc}, v_{ext} and v_H).

2. Using the $v_{eff}(\mathbf{r})$, the KS equations are solved to obtain a new set of orbitals $\psi_i(\mathbf{r})$.

3. Using the new set of orbitals we obtain another electron density (2.26) and this updated density is then used to reconstruct the new v_{eff}.

The cycle then repeats until the input and output densities match - in practice, until they converge within a predefined setting. This self-consistent loop ensures that the final orbitals and density are consistent with the potential they generate [9].

2.2.4 Basis sets and pseudopotentials

In practical calculations, it is essential to represent the KS-orbitals in a finite basis, in order to produce meaningful results. The so-called **basis sets** consist of mathematical functions, that serve as building blocks for the orbitals. Each Kohn-Sham orbital is expressed as a linear combination of basis functions ϕ_ν

$$\psi_n(\mathbf{r}) = \sum_{\nu=1}^{N_b} C_{n\nu}\,\phi_\nu(\mathbf{r}), \tag{2.41}$$

where $C_{n\nu}$ are the molecular orbital coefficients and N_b is the number of basis functions. There are certain requirements for choosing the basis functions. First, they should exhibit behavior appropriate to the physics of the given problem, ensuring the convergence becomes sufficiently rapid as more basis functions are added. This means that the functions should go towards zero with increasing distance of the electron from the nucleus. Another requirement is practical: The chosen function ideally should allow efficient computation of all the required integrals. The two most commonly used basis functions are *Slater Type Orbitals* (STO) and *Gaussian Type orbitals* (GTO), although the GTOs are generally preferred in the calculations of electronic structures, due to the ease they provide in calculations. Although the rough guideline suggests that up to three times as many GTOs than STOs are required to achieve the same level of accuracy and despite them having a poorer r^2 dependence, these disadvantages are more than compensated by the considerable amount of computational efficiency they offer. Gaussian Type orbitals have the form

$$\chi_{\xi,n,l,m}(r,\theta,\phi) = N Y_{l,m}(\theta,\phi)\, r^{2n-2-l}\, e^{-\xi r^2} \tag{2.42}$$

where N is the normalization constant, $Y_{l,m}$ are spherical harmonics, r^{2n-2-l} is the radial prefactor and the exponential term describes the distance dependence [6]. In our work, the Kohn-Sham orbitals were expanded using the Gaussian DZVP-MOLOPT basis set [11] for efficiency and in accordance with previous studies in this field [1].

In addition to representing the orbitals, it is also necessary to properly deal with the Coulomb contribution of the atomic nuclei and the inner core electrons. We can, by eliminating the core electron wave functions, reduce the number of orbitals that must be considered in the calculations. This is where the **pseudopotentials** come into play. They replace the effect of the nuclei and core electrons with an effective, smoother potential. From a chemical perspective, explicitly calculating for large numbers of core electrons in systems involving third-row or heavier elements from the periodic table is unnecessary [6]. Formally, this contribution belongs to the external potential v_{ext} in the Kohn-Sham equations. Pseudopotentials ease the calculations drastically by reducing the size of basis sets used [12]. We used a dual-space, norm-conserving Goedecker–Teter–Hutter pseudopotential [12] in this work, treating the single Na $3s^1$ electron. For comparison, some calculations also included the 9

Na $2s^2 2p^6 3s^1$ electrons. "Norm-conserving" here means that the norm of the pseudo wave function matches the norm of the all-electron wave function inside the core region [13].

2.2.5 Approximations to the exchange-correlation functional

As mentioned earlier, the exchange-correlation potential is formally obtained as the functional derivative of the exchange-correlation functional

$$v_{xc}(\mathbf{r}) = \frac{\delta E_{xc}[n]}{\delta n(\mathbf{r})}. \tag{2.43}$$

A "functional derivative" can be understood similarly to the regular derivative: it measures the sensitivity of a functional to a small variation of its variable (here the electron density). The following theorem summarizes how the functional derivative is computed [2]:
For a given functional

$$F[n] = \int f(\mathbf{r}, n(\mathbf{r}), \nabla n(\mathbf{r}))\, d^3r, \tag{2.44}$$

the functional derivative can be computed as

$$\frac{\delta F}{\delta n(\mathbf{r})} = \frac{\partial f}{\partial n} - \nabla \cdot \left(\frac{\partial f}{\partial (\nabla n)} \right). \tag{2.45}$$

The exact form of $E_{xc}[n]$ is unknown, therefore, we rely on approximation methods in practical calculations.

Local density approximation (LDA)

The simplest approximation for E_{xc} is the local density approximation (LDA), originally proposed by Kohn and Sham. It is based on the idea that the electron density at each point in space can be treated as if it were part of a homogeneous electron gas [4]. In LDA, E_{xc} is approximated as

$$E_{\mathrm{xc}}^{\mathrm{LDA}}[n] = \int d^3r\, f(n(\mathbf{r})), \tag{2.46}$$

where $f(n)$ is simply a function of density (not a functional), depending on the local value of the density n. While fairly easy to implement, in reality, LDA typically underestimates exchange-correlation energies of atoms and molecules [14].

Generalized gradient approximation (GGA)

A substantial improvement is achieved by **Generalized Gradient Approximation (GGA)**, which incorporates not only the electron density but also its gradient $\nabla n(\mathbf{r})$ into the functional. This, in comparison with LDA, also describes how strongly the electron density $n(\mathbf{r})$

varies in space [2]

$$E_{\mathrm{xc}}^{\mathrm{GGA}}[n] = \int d^3r\, f(n(\mathbf{r}), \nabla n(\mathbf{r})). \tag{2.47}$$

GGAs improve the accuracy of total energies, energy barriers and structural energy differences and favor more realistic inhomogeneous densities. One of the widely used GGA exchange-correlation potentials is the **Perdew-Burke-Ernzerhof (PBE)** [15], which is also employed in our work within the adiabatic approximation (we will discuss the adiabatic approximation in more detail in the next chapter. It successfully achieves a balance between computational efficiency and good accuracy. For its detailed form and derivation we refer the reader to the literature [4, 15], as its derivation requires extensive theoretical background.

Beyond the methods mentioned above, more advanced classes of functionals have been developed, such as **hybrid functionals** (e.g. B3LYP, PBE0) or **meta-GGA functionals** [4], with chemical accuracy exceeding that of GGAs or LDAs [16]. The choice of the functional depends on the goal and available computational resources.

Chapter 3

From time-dependent DFT to spectra

Electronic dynamics takes place on extremely short timescales: it ranges from attoseconds to a few hundred femtoseconds (see Fig. 3.1). In contrast, nuclear motion is much slower than that of electrons due to their larger mass. Nuclear motion underlies the formation or breaking of chemical bonds, the rearrangement of functional groups and the timescale of chemical reactions. These processes can last hundreds of picoseconds, depending on the size and complexity of the system.

Formally, the motion of electrons and nuclei is described by a coupled Schrödinger equation for the electronic and nuclear degrees of freedom. Such calculations are only realistically solvable for very small systems. While in practice the electron dynamics is treated fully quantum mechanically, nuclear degrees of freedom are often treated classically. Throughout this work, we assume that the nuclei remain fixed during the electronic dynamics according to the Born-Oppenheimer approximation.

The most crucial tool introduced in this chapter is the time-dependent density functional theory (TDDFT), which mainly focuses on electronic excitation processes and their associated time evolution in atoms, molecules and condensed matter systems. TDDFT provides a framework that is fairly accurate and practical at the same time, linking the time-resolved dynamics directly to the measurable quantities and thereby bridging theory with spectroscopic methods [4].

In this chapter, we first introduce the most intuitive quantities that can be computed from the time-dependent density, such as particle number, before turning to dynamical dipole moments, dipole power spectrum with examples and the widely used photoabsorption and emission spectroscopies, together with their theoretical treatment. We then discuss the essential elements of the linear response theory, which theoretically ties these observables to excitation spectra.

Linear response is valid when the external perturbing field is weak compared to the electrostatic field created by the nuclei (on the order of $10^{10}\,\mathrm{V/m}$). Within the linear regime, we will see that the spectral behavior is independent of the perturbation strength and that the linear response contains all the spectral features.

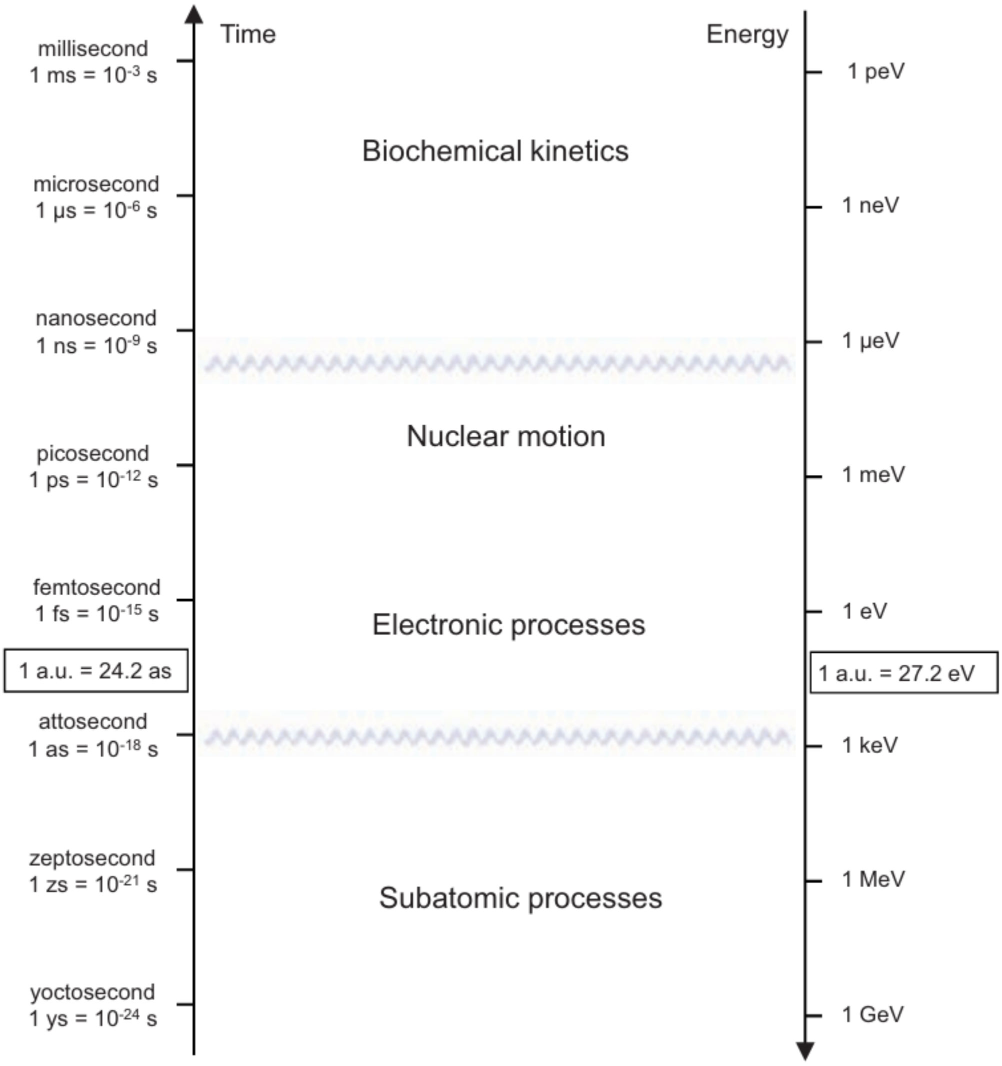

Figure 3.1: Characteristic processes of nature, such as biochemical kinetics, nuclear motion, electronic processes and subatomic processes with their associated time (left axis) and energy (right axis) scales, both given in atomic units (a.u.) of time and energy. For our purposes, the relevant range here spans from tens of attoseconds to a few hundred femtoseconds. Adapted from [4].

This chapter is mainly based on the book by Carsten A. Ullrich [4], complemented by the logical structure and physical formulations of Jan Wilhelms Lecture Notes [2] and additional literature references are given where appropriate.

3.1 Time-dependent density functional theory

TDDFT extends the concepts of static DFT to dynamical processes. It enables the description of electronic excitations and their response to external electric fields, such as laser pulses. Its foundations are provided by the Runge–Gross theorem and the van Leeuwen theorem, which lead to the practical formulation of the time-dependent Kohn-Sham scheme.

3.1.1 Time-dependent many-electron problem

In quantum mechanics, the dynamics of a many-body problem is governed by the time-dependent Schrödinger equation

$$i\frac{\partial}{\partial t}\Psi(\mathbf{r}_1,\dots,\mathbf{r}_N,t) = \hat{H}(t)\Psi(\mathbf{r}_1,\dots,\mathbf{r}_N,t). \tag{3.1}$$

As in the static case, we assume the Born-Oppenheimer approximation to be valid, i.e., the nuclei are fixed. Here, Ψ is the time-dependent wave function describing the time evolution of the N-electrons system. The Hamiltonian is composed of, as in the static case, the kinetic energy, the electron-electron and electron-nuclei interaction potentials and additionally the time-dependent external potential operator $\hat{V}(t)$

$$\hat{H}(t) = \hat{H}_0 + \hat{V}(t)\,\theta(t-t_0), \tag{3.2}$$

with H_0

$$\hat{H}_0 = -\frac{\hbar^2}{2m}\sum_i \nabla^2_{\mathbf{r}_i} - \sum_A\sum_{j=1}^{N}\frac{Z_A e^2}{|\mathbf{r}_j-\mathbf{R}_A|} + \sum_i\sum_{j>i}\frac{e^2}{|\mathbf{r}_i-\mathbf{r}_j|}. \tag{3.3}$$

The time-dependent external potential $\hat{V}(t)$ is given as a sum over the contributions of all N electrons interacting with the external field

$$\hat{V}(t) = \sum_{j=1}^{N} v(\mathbf{r}_j,t), \tag{3.4}$$

with the time-dependent external scalar potential being

$$v(\mathbf{r},t) = -e\,\mathbf{r}\cdot\mathbf{E}(t). \tag{3.5}$$

Here, $E(t)$ is the applied electric field, e the elementary charge and $\mathbf{r}$ the position vector. When the time-dependent potential $\hat{V}(t)$ is switched on at time t_0, the initial many-electron state is perturbed and with the initial state $\Psi(\mathbf{r_1},...,\mathbf{r}_N,t_0) = \Psi_0(\mathbf{r_1},...,\mathbf{r}_N)$ provided, solving the Schrödinger equation (3.1) yields $\Psi(\mathbf{r_1},...,\mathbf{r}_N,t)$ for all $t \geq t_0$. If it were not for the exponentially growing computational nature of this problem, as already discussed in section 2.2, one could, in principle, obtain the complete information about the system by computing the expectation value for any observable $\hat{O}$

$$O = \langle \Psi(\mathbf{r}_1, \ldots, \mathbf{r}_N, t) \,|\, \hat{O} \,|\, \Psi(\mathbf{r}_1, \ldots, \mathbf{r}_N, t) \rangle. \tag{3.6}$$

This challenge motivates the search for more efficient approaches based on a simpler quantity than the full many-body solution.

Runge-Gross Theorem

An important extension of DFT to time-dependent systems is provided by the Runge-Gross theorem (RGt). Just as the Hohenberg-Kohn theorems reformulated ground state quantum mechanics in terms of the electron density, Runge and Gross (1984) established the corresponding framework for the time-dependent systems. Formally, the RGt [17] is illustrated as

$$n(\mathbf{r}, t) \text{ and } \Psi_0 \xrightarrow{\text{RGt}} v(\mathbf{r}, t). \tag{3.7}$$

Physically, this means that for a given initial state Ψ_0, the time-dependent electron density $n(\mathbf{r}, t)$ uniquely determines the time-dependent external potential $v(\mathbf{r}, t)$ (up to a purely time-dependent constant). As a corollary, the theorem also implies that the time-dependent density $n(\mathbf{r}, t)$, together with the initial many-electron state Ψ_0, is sufficient to determine the full time evolution $\Psi(t)$ of the system. Consequently, all expectation values of observables $O(t)$ can be obtained solely from Ψ_0 and $n(\mathbf{r}, t)$ [2]

$$n(\mathbf{r}, t),\, \Psi_0 \xrightarrow{\text{RGt}} v(\mathbf{r}, t) \xrightarrow[\Psi_0 \text{ given}]{(3.1)} \Psi(t) \xrightarrow{(3.6)}, O(t) \tag{3.8}$$

or formulated briefly

$$O(t) = [n(\mathbf{r}, t), \Psi_0](t). \tag{3.9}$$

This denotes that any time-dependent observable $O(t)$ can formally be written as a functional of the time-dependent density and the initial state Ψ_0, hence, the name *time-dependent density functional theory*. Proof for the unique mapping between $n(\mathbf{r}, t)$ and the potentials can be found in standard references on TDDFT [4] as well as in the original work of Runge and Gross [17].

3.1.2 Time-dependent Kohn-Sham scheme

The Runge-Gross theorem already established a solid foundation for TDDFT by guaranteeing that the time-dependent density, in combination with the initial state, sets all the observables, i.e., it determines their values uniquely. For practical applications, however, this ansatz is of limited use, since it would require directly solving the many-electron time-dependent Schrödinger equation. An efficient approach is needed that still provides the correct time-dependent density.

This is where the theorem proved by van Leeuwen (1999) [18] enters the picture. It establishes that there exists a non-interacting reference system which reproduces the same density, provided the initial state and density are chosen correctly. This construction is analogous to the Kohn-Sham DFT. On this basis, one can formulate the time-dependent Kohn-Sham scheme (TDKS): instead of propagating the complicated many-body wave function, one propagates a set of single-particle orbitals whose combined density reproduces the real many-body density. The TDKS scheme is summarized as follows:

1. **Initialization**

   Assume that the many-electron system in an external potential of the nuclei is initially in the ground state up to time t_0. By solving the Kohn-Sham equations (2.37) we find the associated Kohn-Sham orbitals $\phi_i(\mathbf{r})$

   $$\left[-\frac{\hbar^2}{2m}\nabla^2 + v_H[n_0](\mathbf{r}) + v_{xc}^0[n_0](\mathbf{r}) + v_{ext}(\mathbf{r})\right]\phi_i(\mathbf{r}) = \varepsilon_i\phi_i(\mathbf{r}) \tag{3.10}$$

   and construct the ground state density $n_0(\mathbf{r})$

   $$n_0(\mathbf{r}) = \sum_{i=1}^{N}|\phi_i(\mathbf{r})|^2, \tag{3.11}$$

   with v_{xc}^0 being the ground state exchange-correlation potential.

2. **Set initial conditions**

   Use $\psi_i(\mathbf{r},t_0) = \phi_i(\mathbf{r})$ as the starting point for the time-dependent Kohn-Sham orbitals.

3. **Time propagation**

   For each discrete time step t_j with $j = 0, 1, 2, \ldots$ (starting from t_0) propagate the orbitals $\psi_i(\mathbf{r},t_j)$ using the time-dependent Kohn-Sham equations

   $$\left[-\tfrac{\hbar^2}{2m}\nabla^2 + v_H[n](\mathbf{r},t_j) + v_{xc}[n](\mathbf{r},t_j) + v_{ext}(\mathbf{r}) + v(\mathbf{r},t_j)\right]\psi_i(\mathbf{r},t_j) = i\,\partial_t\psi_i(\mathbf{r},t_j), \tag{3.12}$$

   where $\psi_i(\mathbf{r},t_j)$ are the time-evolving single-particle orbitals at time step t_j. The time-dependent external potential $v(\mathbf{r},t_j)$ that perturbs the initial system, often caused by a time-dependent electric field as given in (3.5).

4. **Density update**

   Compute the density at each time step

   $$n(\mathbf{r},t_j) = \sum_{i=1}^{N}|\psi_i(\mathbf{r},t_j)|^2. \tag{3.13}$$

5. **Potential update**

   Recalculate the potentials from the updated density:

- Hartree potential acquires its time dependence from the electron density

$$v_H[n](\mathbf{r}, t_j) = e^2 \int d^3r' \, \frac{n(\mathbf{r}', t_j)}{|\mathbf{r} - \mathbf{r}'|}. \tag{3.14}$$

- The time-dependent exchange-correlation potential $v_{xc}[n](\mathbf{r}, t_j)$ depends, in principle, on the entire history of the electron densities $n(\mathbf{r}, t'_j)$. This makes it fundamentally different from the ground-state potential $v^0_{xc}[n_0](\mathbf{r})$, which only depends on the ground-state density $n_0(\mathbf{r})$. Since the exact form of $v_{xc}[n](\mathbf{r}, t_j)$ is unknown, we rely on approximations (see section The adiabatic approximation).

This self-consistent propagation ensures that the single-particle orbitals change under an effective potential which generates the right time-dependent density of the interacting system. The TDKS method, therefore, opens up a practical approach for the direct simulation of the time-dependent behavior of many-electron systems exposed to external fields. The next step would be to use the obtained time-dependent density $n(\mathbf{r}, t)$ as an input for computing the physical observables, as we will see in section 3.2.

The adiabatic approximation

A natural method for approximating the time-dependent exchange-correlation potential is to rely on the known results of the static DFT. One takes the ground state exchange-correlation potential $v^0_{xc}[n_0]$ corresponding to the ground state density $n_0(\mathbf{r})$ and simply replaces $n_0(\mathbf{r})$ with the time-dependent density $n(\mathbf{r}, t)$, yielding the adiabatic potential

$$v^A_{\mathrm{xc}}(\mathbf{r}, t) = v^0_{\mathrm{xc}}[n_0](\mathbf{r})\Big|_{n_0(\mathbf{r}) \to n(\mathbf{r}, t)}. \tag{3.15}$$

The term "adiabatic" means that the potential at any given time t depends exclusively on the instantaneous density. Past densities play no role, i.e., there are no "memory effects". Physically, this corresponds to the assumption that the system remains in its instantaneous eigenstate if a perturbation acting on it is slow enough[1].

3.2 Common observables

In the time-dependent simulations, various physical observables can be monitored to gain information about the electronic dynamics of the system. The most straightforward observable is the time-dependent electron density itself. As the name reveals, it offers insight into the electronic distribution as a function of both position and time.

---

[1] "slow enough" here means relative to the intrinsic timescale of the system: As long as the change in perturbation is slower than this timescale, the system can adapt and remain in the instantaneous eigenstate.

The particle number

Another very intuitive global observable is the particle number N, which can be obtained by integrating the time-dependent density over the whole space

$$\int_{\text{all space}} d^3r\, n(\mathbf{r}, t) = N. \tag{3.16}$$

Although it may appear to be a rather simple quantity, it can be of great interest to know the number of particles in a given finite spatial region at a given moment when strong excitations occur. For instance, we might want to know how much charge is being transferred from one region of a cluster to another region. With appropriate computational settings, it is also possible to analyze how much charge density escapes the system following excitation with a laser pulse.

Dipoles and electronic resonances

Time-dependent dipole moment $\boldsymbol{\mu}(t)$ directly follows from the time-dependent density as

$$\boldsymbol{\mu}(t) = \int d^3r\, \mathbf{r}\, n(\mathbf{r}, t), \quad \text{i.e.,} \quad \mu_\alpha(t) = \int d^3r\, r_\alpha\, n(\mathbf{r}, t), \quad \alpha = x, y, z. \tag{3.17}$$

The dipole moment thus describes the shift of the charge distribution over time and reacts directly to external electrical fields, such as a short laser pulse. An illustrative example of this can be found in the work of Calvayrac (1997) [3], which we reproduced in our simulations (see Appendix A for the implementation of a Gaussian laser pulse in TDDFT simulations using CP2K). Figures 3.2a and 3.2b show the time-dependent dipole moment of a Na_9^+ nanoparticle subjected to Gaussian laser pulses with electric field profiles in the x-direction ($\hat{e} = \hat{e}_x$). The pulses were applied with a non-resonant frequency of $\hbar\omega_1 = 2.5\,\mathrm{eV}$ and a resonant frequency of $\hbar\omega_2 = 2.88\,\mathrm{eV}$ respectively. The selection of these excitation energies is based on a spectral dipole power analysis of the nanoparticle, which will be introduced in the following section.

In the non-resonant case (Fig. 3.2a) the dipole moment closely follows the applied laser pulse. In contrast, in the resonant case (Fig. 3.2b) the dipole moment continues to oscillate with a larger amplitude even after the pulse has ended. This behavior indicates that a plasmon mode was excited by applying a laser pulse with the exact resonant energy.

Rather than performing multiple TDDFT simulations across a range of frequencies ω to identify the resonant frequency of a given system, it would be more efficient to obtain the entire spectrum of electronic resonance frequencies with a single TDDFT simulation. This brings us to the next quantity: the dipole power.

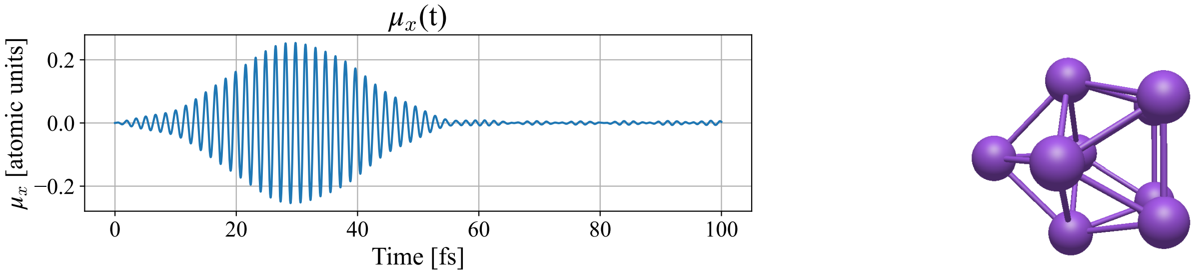

(a) Non-resonant case: $\hbar\omega_1 = 2.5\,\text{eV}$

(c) Na_9^+ nanoparticle structure

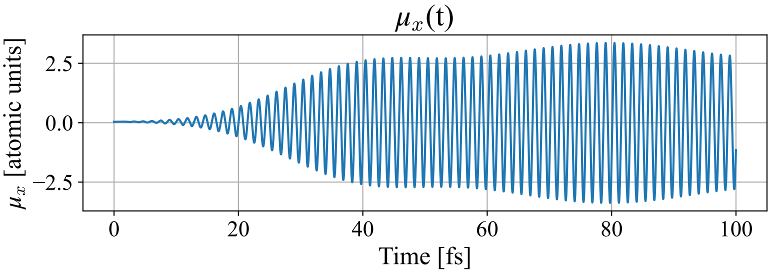

(b) Resonant case: $\hbar\omega_2 = 2.88\,\text{eV}$

Figure 3.2: Time-dependent dipole moments $\boldsymbol{\mu}_x(t)$ (3.17) of a Na_9^+ nanoparticle computed with TDDFT, subject to 25 fs Gaussian laser pulses with peak field $E_0 = 1.9 \cdot 10^6\,\text{V/m}$ and periods $T_1 = 2\pi/\omega_0 = h/2.5\,\text{eV} \approx 1.65\,\text{fs}$ (a) and $T_2 \approx 1.43\,\text{fs}$ (b). The geometric structure of the nanoparticle in Fig. (c) was constructed using the Avogadro software [19]. Simulation length 100 fs in 0.01 fs time steps. Simulated following the example in [3].

Dipole power spectrum

In order to simultaneously cover all possible frequencies at once, the many-electron system must be prepared in all eigenmodes at once. This raises the question: how can this be achieved? A nice everyday analogy can be found in [4], comparing the process to striking a bell. When the bell receives a single sharp blow with a hammer, it starts to resonate with a characteristic combination of the fundamental tone and overtones. The resulting frequency spectrum can be extracted from the sound profile measurement. The bell represents the metal cluster of interest and the hammer in the TDDFT corresponds to a sudden perturbation applied at time $t = t_0$, referred to as a delta pulse (Fig. 3.3)

$$E^{\text{delta}}(t) = \mathcal{I}\delta(t - t_0). \tag{3.18}$$

Here $\delta(t - t_0)$ has the unit 1/time, consequently, the magnitude of the electric-field impulse $\mathcal{I}$ carries units of field×time $(\text{V} \cdot \text{s}/m)$. The Fourier transformation of (3.18) is a constant function $E(\omega) = \mathcal{I}$, meaning all the frequencies are equally represented. After applying the delta pulse, we let the system evolve for some time. One calculates the dipole moment $\boldsymbol{\mu}(t)$ from the time-dependent density as defined in (3.17) and its frequency picture is obtained via Fourier transforms over a finite time window $t_0 < t < t_1$

$$\boldsymbol{\mu}(\omega) = \frac{1}{t_1 - t_0} \int_{t_0}^{t_1} \boldsymbol{\mu}(t)\, e^{-i\omega t}\, dt. \tag{3.19}$$

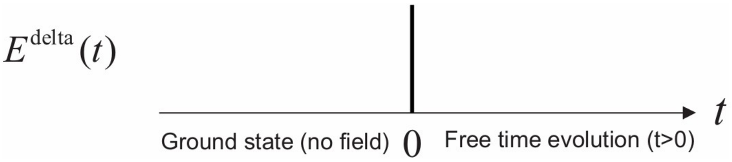

Figure 3.3: Illustration of the electric pulse (3.18) applied at $t_0 = 0$ The vertical line represents the instantaneous perturbation, which excites all frequencies equally. The system is then propagated in the absence of external fields. Adapted from [4].

The quantity $\boldsymbol{\mu}(\omega)$ is closely related to the photoabsorption cross section $\sigma(\omega)$, which will be discussed in the next section. Instead of $\boldsymbol{\mu}(\omega)$, it is in practice convenient to work with the power spectrum $D(\omega)$, a positive definite quantity

$$D(\omega) = |\mu_x(\omega)|^2 + |\mu_y(\omega)|^2 + |\mu_z(\omega)|^2. \tag{3.20}$$

By applying the delta pulse (3.18) to the Na_9^+ nanoparticle, allowing it to propagate over time (see Appendix A for the implementation of delta pulse excitation in TDDFT simulations using CP2K) and evaluating the results with the steps (3.19) and (3.20) results in the dipole power spectrum shown in Fig. 3.4.

The pronounced resonant peak at 2.88 eV (obtained via $E = \hbar\omega$), which is known as Mie (surface) plasmon, agrees well with the value in the literature [3]. Few spectral features of much smaller intensity are also visible, which correspond to single-particle excitations and bulk-like higher excitations. This spectrum explains why the nanoparticle responded so "favorably" to the gaussian pulse carrying the resonant energy and a pulse with non-resonant energy failed to couple effectively to the system.

The reasonable accuracy of our results gives us confidence in the accuracy of our TDDFT algorithms and other processing tools for the rest of our work. The slight deviation in the value of the plasmon energy compared to the original work may be attributed to the differences in the exchange-correlation functional: the original work incorporates the adiabatic local density approximation (ALDA), while our simulations employ PBE in adiabatic approximation.

It should be noted that the numerical evaluation of $\mu_\alpha(\omega)$ tends to introduce spurious noise into the spectrum, because it cuts out a finite time slice of a signal that is assumed to be periodic. In practical calculations, however, it is recommended to use some form of window function during the Fourier transformation over a finite sampling interval. Throughout our calculations, we used the cosine filtering where the data are multiplied with a factor $cos^2(t\pi/2T)$ following the approach of Calvayrac [3].

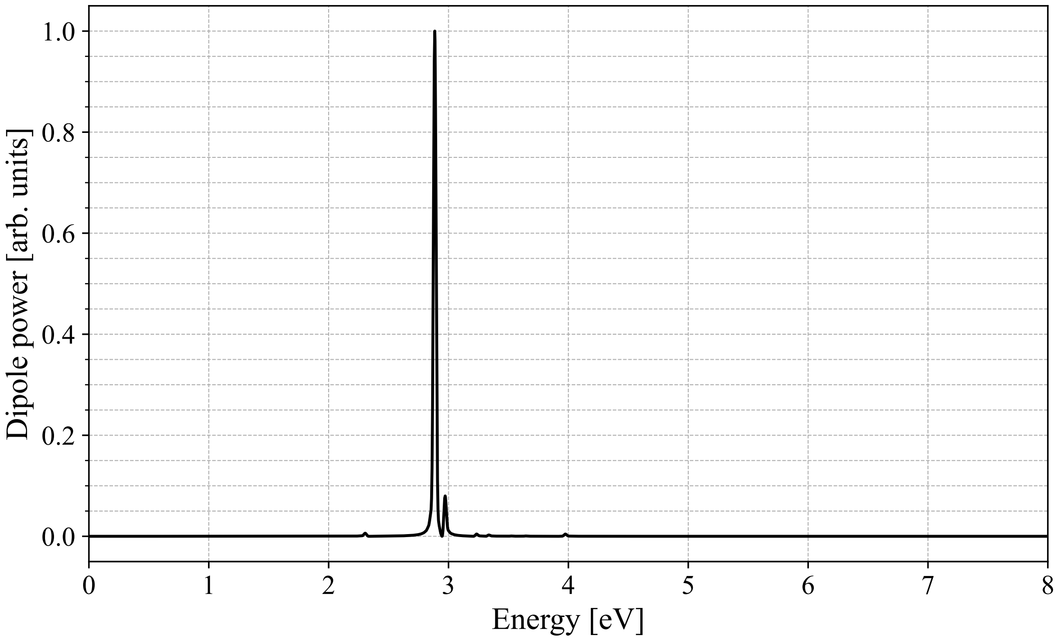

Figure 3.4: Normalized dipole power spectrum (3.20) of the Na_9^+ nanoparticle, plotted as a function of energy via $E = \hbar\omega$. A sharp resonance at 2.88 eV is visible following a delta pulse excitation of 0.01 a.u. magnitude. Computed using TDDFT in CP2K. Simulation length 200 fs in 0.01 fs time steps. Simulated following the example in [3].

Emission spectrum

The applicability of the dipole moment $\boldsymbol{\mu}(t)$ extends beyond the dipole power spectrum. In techniques such as NOTE microscopy [1], the emitted electromagnetic radiation from accelerated electrons in the near-field provides valuable information about the underlying electron dynamics. Put simply, the dipole moment describes the position of the charges and by extension, its second derivative $\frac{\partial^2 \boldsymbol{\mu}(\boldsymbol{t})}{\partial t^2}$ corresponds to the acceleration of charges. The spectral emission power $I(\omega)$ radiated from the accelerated electrons of a many-electron system is then given by (with $k = \omega/c$, where c is the speed of light)

$$I(\omega) = \frac{1}{3c^3} |\omega^2 \boldsymbol{\mu}(\omega)|^2. \tag{3.21}$$

Here, the prefactor arises from the Fourier transformation of $\partial^2 \boldsymbol{\mu}(\boldsymbol{t})/\partial t^2$. This formulation enables the calculation of the emission spectrum in NOTE microscopy and related nano-optical techniques [2, 20].

3.3 Optical absorption spectrum and excitation energies

Optical absorption spectroscopy is one of the fundamental methods for analyzing matter, both qualitatively and quantitatively. In a typical experiment, a sample is irradiated and the absorbed intensity is recorded for each frequency. The resulting absorption spectrum provides direct access to the excitation energies, since absorption occurs when the photon energy matches exactly the energy difference between the ground state and the excited state [21]. An example is shown in the Fig 3.5. Such spectra can be used not only to identify materials involved in the sample, but in some cases also to determine their quantity [2].

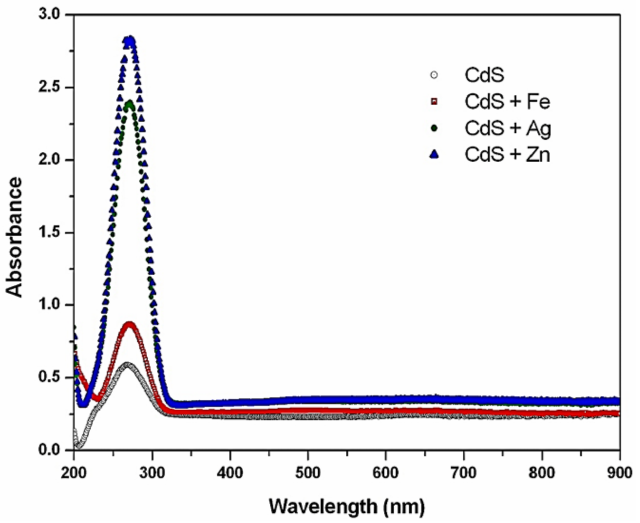

Figure 3.5: Comparison of absorption spectra for undoped and metal-doped CdS quantum dots. Adapted from [22].

Let us now examine how absorption spectra can be computed using TDDFT and how this is related to the observations from the previous section. For this purpose, we look into the linear response theory, without going into excessive detail. Linear response applies when the external field is sufficiently weak (compared to the electrostatic field of the nuclei). The linear density response is given by

$$n_1(\mathbf{r},t) = \int_{-\infty}^{\infty} dt' \int d^3r' \, \chi_{nn}(\mathbf{r},\mathbf{r}',t-t') \, v(\mathbf{r}',t'), \tag{3.22}$$

where the density-density response function χ is defined as

$$\chi_{nn}(\mathbf{r},\mathbf{r}',t-t') = -\theta(t-t')\langle\Psi_0 \,|\, [\hat{n}(\mathbf{r},t-t'),\hat{n}(\mathbf{r}')] \,|\, \Psi_0\rangle. \tag{3.23}$$

Here, $\hat{n}(\mathbf{r},t)$ represents the time-dependent density operator and Ψ_0 is the ground state of the system. The commutator $[\hat{n}'(\mathbf{r},t-t'),\hat{n}(\mathbf{r})]$ quantifies how the density at position $\mathbf{r}$ and time t is affected by a prior fluctuation of the density at r' and t'. The expectation value $\langle\Psi_0 \,|...|\, \Psi_0\rangle$ averages this effect over the ground state. The Heaviside function $\theta(t-t')$ ensures causality, i.e., only if the perturbation occurs at an earlier time t' does it contribute to the response. This response is independent of the explicit form of the perturbation $v(\mathbf{r},t)$. Importantly, the χ_{nn} quantifies how strongly the density at one point in space and time reacts to a perturbation of the density at another point in space and an earlier time.

The frequency-domain representation of this response function reads

$$\chi_{nn}(\mathbf{r},\mathbf{r}',\omega) = \lim_{\eta\to 0^+} \sum_{n=1}^{\infty} \left(\frac{\langle\Psi_0|\hat{n}(\mathbf{r})|\Psi_n\rangle\langle\Psi_n|\hat{n}(\mathbf{r}')|\Psi_0\rangle}{\omega - \Omega_n + i\eta} - \frac{\langle\Psi_0|\hat{n}(\mathbf{r}')|\Psi_n\rangle\langle\Psi_n|\hat{n}(\mathbf{r})|\Psi_0\rangle}{\omega + \Omega_n + i\eta} \right). \tag{3.24}$$

The key quantity for us in this relation is the frequency Ω_n, which corresponds to the energy required to excite the many-electron system from ground state Ψ_0 to excited state Ψ_n, with definition $\Omega_n = E_n - E_0$ ($\hbar = 1$ in atomic units). A strong response occurs in the resonant case, i.e., when the frequency of the external electromagnetic radiation matches the excitation energy $\omega = \Omega_n$.

The external perturbation is taken as an oscillating field with a linear polarization along the axis r_μ ($\mu = 1, 2, 3, r_1 \equiv x, r_2 \equiv y, r_3 \equiv z$)

$$v(\mathbf{r},t) = -e\, r_\mu E_0\, e^{-i\omega t}. \tag{3.25}$$

The optical absorption probability of light of frequency ω, as measured in optical spectra, is proportional to the photoabsorption cross section

$$\sigma_{\mu\mu}(\omega) = \frac{4\pi\omega}{c} \operatorname{Im} \alpha_{\mu\mu}(\omega), \tag{3.26}$$

with c being the speed of light and $\alpha_{nn}(\omega)$ the polarizability of the many-electron system. The polarizability can be defined as the proportionality constant relating the external electric field to the polarization of the system

$$p_\mu(\omega) = \alpha_{\mu\mu}(\omega)\, E_\mu(\omega). \tag{3.27}$$

Polarization as a response to the electric field can also be expressed in terms of density

$$p_\mu(\omega) = \int d^3r\, r_\mu\, n_1(\mathbf{r},\omega). \tag{3.28}$$

In the linear response theory, one considers the change in the density $n_1(\mathbf{r},\omega)$ caused by an external field. This induces a polarization $p_\mu(\omega)$, which formally has the same structure as the dipole moment from the previous section, but is given in the frequency space and restricted to the linear response contribution. Thus, one can interpret the polarization $p_\mu(\omega)$ as the Fourier transformed linear component of the time-dependent dipole moment $\mu(t)$. The density response $n_1(\mathbf{r},t)$ can then be computed using Eqs. (3.22) and (3.25)

$$n_1(\mathbf{r},t) = \int d^3\mathbf{r}'\, \chi_{nn}(\mathbf{r},\mathbf{r}',\omega)\, v(\mathbf{r}',\omega) = -eE_0 e^{-i\omega t} \int d^3\mathbf{r}'\, \chi_{nn}(\mathbf{r},\mathbf{r}',\omega)\, \mathbf{r}'_\mu. \tag{3.29}$$

Inserting this relation into (3.28) yields

$$p_\mu(\omega) = -e\,E_\mu(\omega)\int d^3r\,d^3r'\,r_\mu\,r'_\mu\,\chi_{nn}(\mathbf{r},\mathbf{r}',\omega) = -e\,E_\mu(\omega)\sum_{n=1}^{\infty}\frac{2\Omega_n\,|\langle\Psi_0|\hat{r}_\mu|\Psi_n\rangle|^2}{(\omega+i\eta)^2-\Omega_n^2}. \quad (3.30)$$

So, for the sufficiently weak perturbation, one therefore expects direct linear dependence of the polarization on the field magnitude. By comparing (3.30) to (3.27) we obtain the following relation for polarizability

$$\alpha_{\mu\mu}(\omega) = -e\sum_{n=1}^{\infty}\frac{2\Omega_n\,|\langle\Psi_0|\hat{r}_\mu|\Psi_n\rangle|^2}{(\omega+i\eta)^2-\Omega_n^2} \quad (3.31)$$

and consequently, the absorption probability for light of frequency ω (the absorption cross section) is proportional to

$$\sigma_{\mu\mu}(\omega) = -\frac{4\pi e\omega}{c}\sum_{n=1}^{\infty}\mathrm{Im}\left[\frac{2\Omega_n\,|\langle\Psi_0|\hat{r}_\mu|\Psi_n\rangle|^2}{(\omega+i\eta)^2-\Omega_n^2}\right]. \quad (3.32)$$

This result is crucial, as it shows that resonant driving frequencies which appear in the optical absorption spectrum of the matter correspond to excitation energies $\omega = \pm\Omega_n$. As shown in (3.30), the same conclusion is also valid in the case when computing dipoles from the density response to the polarization: peaks appear at the resonant frequencies. However, in most of our calculations, we perturb the system with a delta pulse (3.18). This corresponds to $E^{\mathrm{delta}}(t) = \mathcal{I}\delta(t-t_0)$, whose Fourier transform is a constant $E(\omega) = \mathcal{I}$ in frequency space. Thus, instead of testing a single driving frequency, the system is excited at all frequencies simultaneously. The subsequent time evolution of the dipole moment contains contributions from all resonant modes Ω_n. By Fourier transforming $\mu(t)$, one directly recovers the absorption spectrum, with peaks located at the excitation energies. In the case of delta pulse excitation, the polarization $p_\mu(\omega)$ takes the form

$$p_\mu(\omega) = \alpha_{\mu\mu}(\omega)\mathcal{I}e^{i\omega t_0}, \quad (3.33)$$

showing explicitly that the polarization is *linearly* proportional to the pulse magnitude $\mathcal{I}$. For instance, when comparing the $\mu_x(t)$, $\mu_x(\omega)$ and the dipole power spectra $D(\omega)$ for the Na_9^+ nanoparticle excited with delta pulses of 0.0001 a.u. (Fig. 3.6) and 0.0002 a.u. (Fig. 3.7) in the x-direction, we observe that $\mu_x(t)$ and $\mu_x(\omega)$ scale with the changing pulse magnitude by a factor of 2 and the dipole power is enhanced by a factor of 4, as it grows quadratically (3.20). Importantly, the spectral behavior remains unaffected, because the spectral features are governed by $\alpha_{\mu\mu}$ in the linear regime.

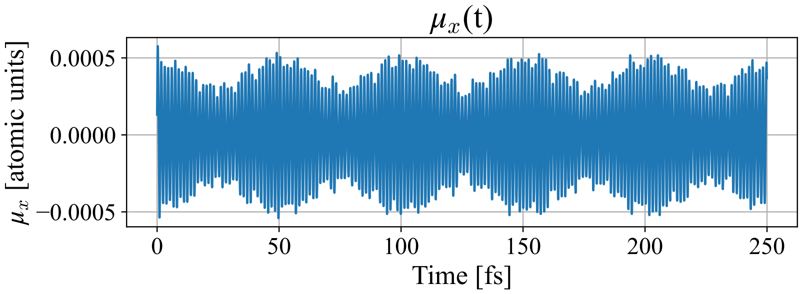

(a) Time-dependent dipole moment oscillation (3.17).

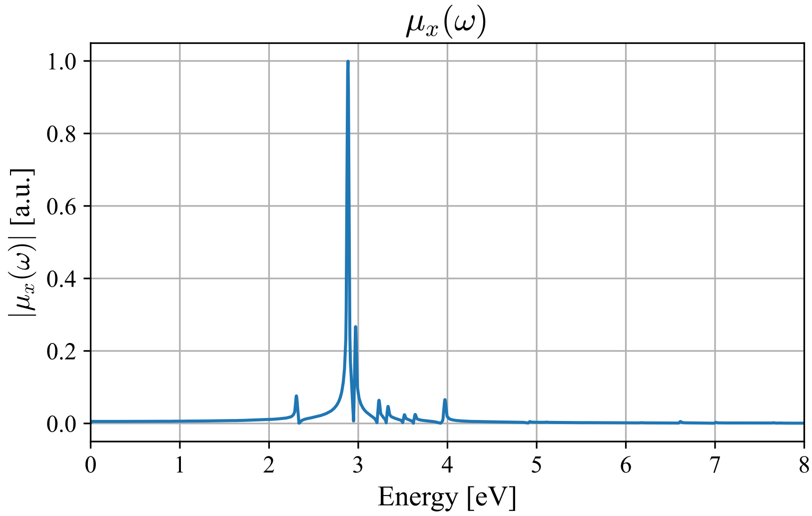

(b) Fourier transform of $\mu_x(t)$ (3.19), plotted as a function of energy via $E = \hbar\omega$.

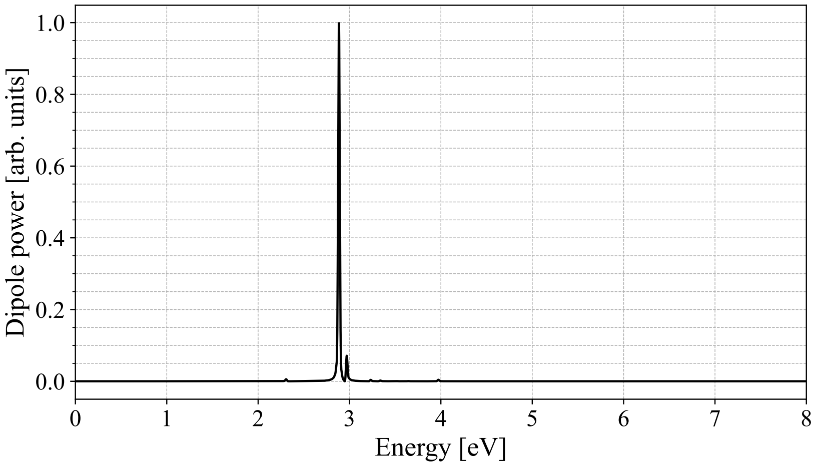

(c) Dipole power spectrum (3.20), plotted as a function of energy via $E = \hbar\omega$.

Figure 3.6: Excitation of Na_9^+ by a delta pulse of 0.0001 a.u. magnitude. Simulation length 250 fs in 0.05 fs time steps.

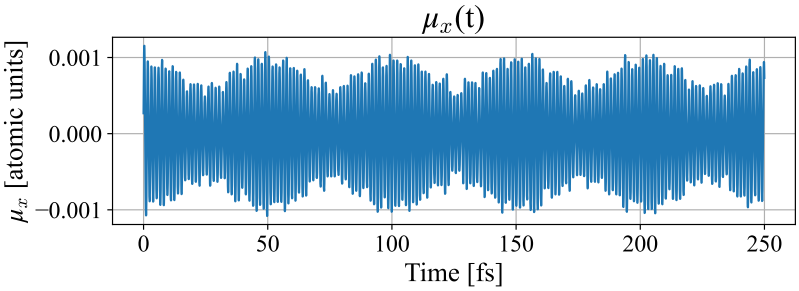

(a) Time-dependent dipole moment oscillation (3.17).

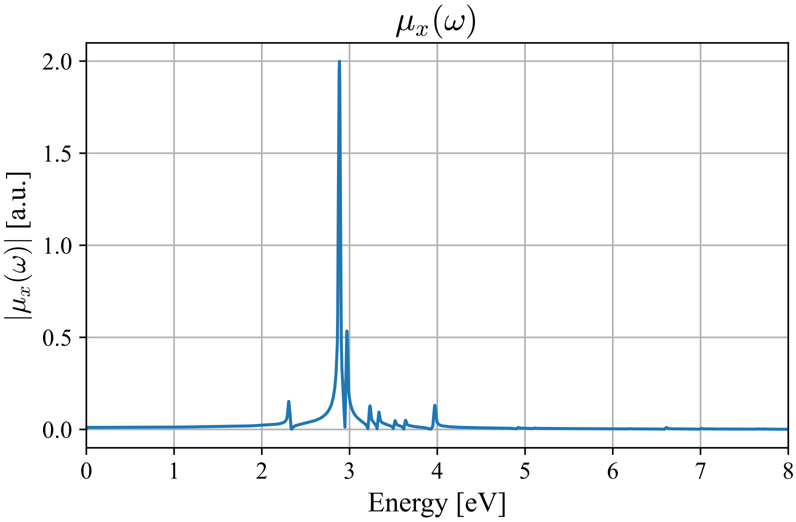

(b) Fourier transform of $\mu_x(t)$ (3.19), plotted as a function of energy via $E = \hbar\omega$.

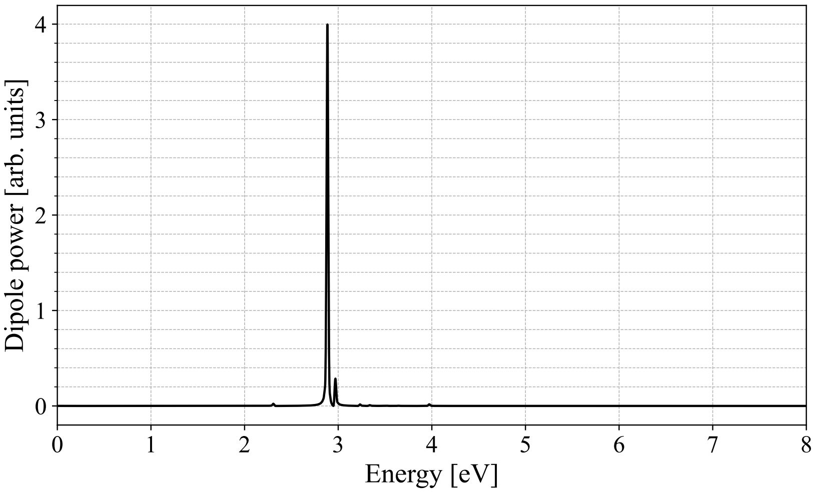

(c) Dipole power spectrum (3.20), plotted as a function of energy via $E = \hbar\omega$.

Figure 3.7: Excitation of Na_9^+ by a delta pulse of 0.0002 a.u. magnitude. Simulation length 250 fs in 0.05 fs time steps.

Chapter 4

Excitation Spectra of Metallic Tip-Substrate Nanostructures

In Chapter 3 we showed that the dipole power spectrum exhibits peaks corresponding exactly to the electronic excitation energies $\Omega_n = E_n - E_0$. In this chapter, we apply the same real-time TDDFT protocol to metallic tip-substrate assemblies that are aligned along the z axis. We first compute and discuss the excitation spectra of a tip-substrate structure using two different pseudopotentials and analyze the spectral changes caused by systematic variation of tip and substrate sizes at fixed alignment and distance. Later, we change the tip-substrate separation distance across different metal clusters and provide physical interpretation of the observed trends.

4.1 Methods and parameters

The overall procedure can be summarized as follows:

1. We excite the sytem with a delta-kick (Polarization vector (0,0,1), since this is the direction of interest for scanning tunneling microscopy geometries). The impulse strength is 0.001 a.u. and it is well within the linear regime. Verification is provided in the Appendix B.

2. Propagate with a time step of 0.02 fs for a total duration of 500 fs. For the clusters considered here, this simulation length is sufficient for the peak positions and their relative intensities to stabilize. To convince the reader, representative convergence tests for some of the clusters used in this work are also listed in the Appendix B.

3. Compute the time-dependent dipole moment for each time step from the time-dependent electron density.

4. Obtain the dipole power spectrum from the time-dependent dipole moment and present it on an energy axis via $E = \hbar\omega$.

For this purpose, we model metallic rectangular-box substrates and square-pyramidal tips composed of Na atoms (body-centered-cubic lattice, lattice constant 0.428 nm). Tips and substrates are aligned along the z axis with total heights approximately between 1 and 3 nm. We choose Na atoms, instead of other metals that are used in real setups (W, Au, etc.), as it considerably reduces the computational costs, while accurately describing generic metallic behavior [23]. All clusters were constructed using the Avogadro software [19].
Tip-substrate clusters are denoted with x atoms in the tip and y atoms in the substrate as $\mathrm{Na}_{x,y}$, e.g. $\mathrm{Na}_{14,34}$ (tip 14 atoms, substrate 34 atoms). Clusters containing only one component are denoted with one index corresponding to the number of atoms, for example, Na_{14}.

4.2 Effect of pseudopotential choice on the excitation spectrum

We start from the $\mathrm{Na}_{14,34}$ cluster as a reference system with a 10 Å gap between the tip and the substrate (in Fig. 4.1). Its normalized dipole power spectra are given in Fig. 4.2, computed with GTH-PBE-q1 and GTH-PBE-q9 pseudopotentials.

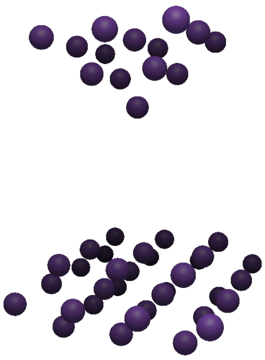

Figure 4.1: $\mathrm{Na}_{14,34}$ cluster with 10 Å gap.

Both spectra exhibit features within the same frequency range, with a pronounced peak at 3.8 eV. The differences in the peak heights within a single spectrum are due to different transition dipole contributions, which is the numerator of the polarizability (3.31). In the spectrum, where the GTH-PBE-q1 pseudopotential is employed in the calculation, the response is dominated by collective oscillations of the explicitly treated $3s^1$ valence electrons. For comparison, in the spectrum computed with the GTH-PBE-q9 pseudopotential, i.e., with 9 electrons explicitly treated per Na atom, additional spectral features appear, as more electrons per atom are included, but the dominant peak at 3.8 eV and the overall energy range remain essentially unchanged. This supports the use of the GTH-PBE-q1 pseudopotential for efficient qualitative analysis of the plasmonic responses for the rest of this work.

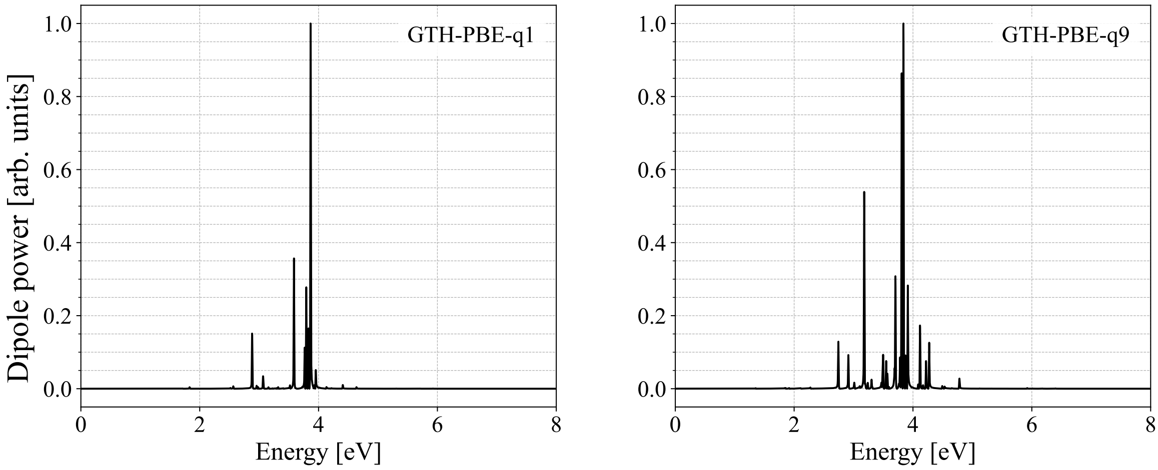

Figure 4.2: Normalized dipole power spectra of the $\mathrm{Na}_{14,34}$ cluster, computed with GTH-PBE-q1 (left) and GTH-PBE-q9 (right) pseudopotentials.

4.3 Excitation spectra as a function of tip and substrate size

At first glance, the spectra shown in Fig. 4.2 remain ambiguous and do not provide clear indications of where the observed resonances occur. We therefore try to disentangle tip- and substrate-dominated features by adding another atomic layer at the tip apex, generating the series of clusters with increasing tip sizes shown in Fig. 4.3. The corresponding spectra (Fig. 4.4) of these clusters reveal clear size-dependent confinement effects: as the tip size increases, several features shift and are reweighted. Interestingly, the pronounced peak at 3.8 eV remains essentially fixed within a few hundredths of an eV. This suggests that it is only weakly affected by the tip geometry.

To rationalize the observed spectra, we adopt a minimal "particle-in-a-3D-box" model for the two metallic parts: the substrate (Box 1) and the tip (Box 2). Each box is given as an infinite 3D well with edge lengths L_x, L_y, L_z and eigenenergies

$$E_{n_x n_y n_z}(L_x, L_y, L_z) = \frac{\hbar^2 \pi^2}{2m} \left(\frac{n_x^2}{L_x^2} + \frac{n_y^2}{L_y^2} + \frac{n_z^2}{L_z^2} \right), \tag{4.1}$$

where $n_x, n_y, n_z \in \mathbb{N}$ are the principal quantum numbers [24]. Initially, Box 1 (substrate) and Box 2 (tip) are cubic with side lengths a and b, respectively. Then we elongate the tip in one dimension: $L_z^{(\mathrm{tip})} : b \to 1.5\, b$ (with $L_x = L_y = b$). This structural change lowers all levels in Box 2 (tip) (the z term scales as $1/L_z^2$) and as a consequence, the transition energies shift. Conversely, features associated with Box 1 (substrate) remain unchanged. The near-invariance of the peak at 3.8 eV under tip-size variation, therefore, hints at a substrate-dominated origin.

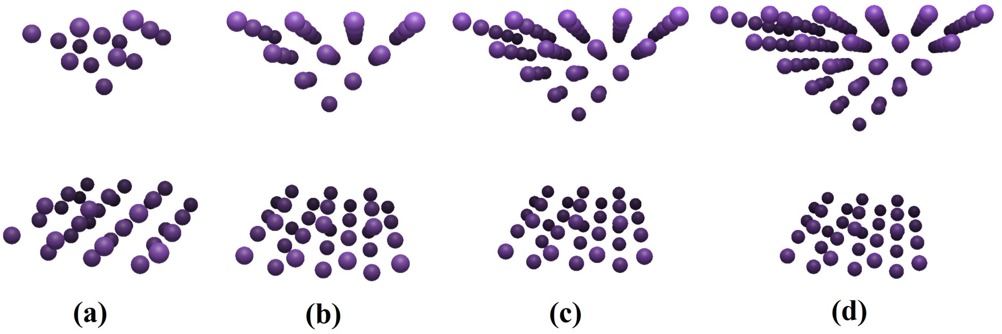

Figure 4.3: Tip-substrate clusters with increasing tip size at 10 Å gap separation: (a) $Na_{14,34}$; (b) $Na_{30,34}$; (c) $Na_{55,34}$; (d) $Na_{91,34}$.

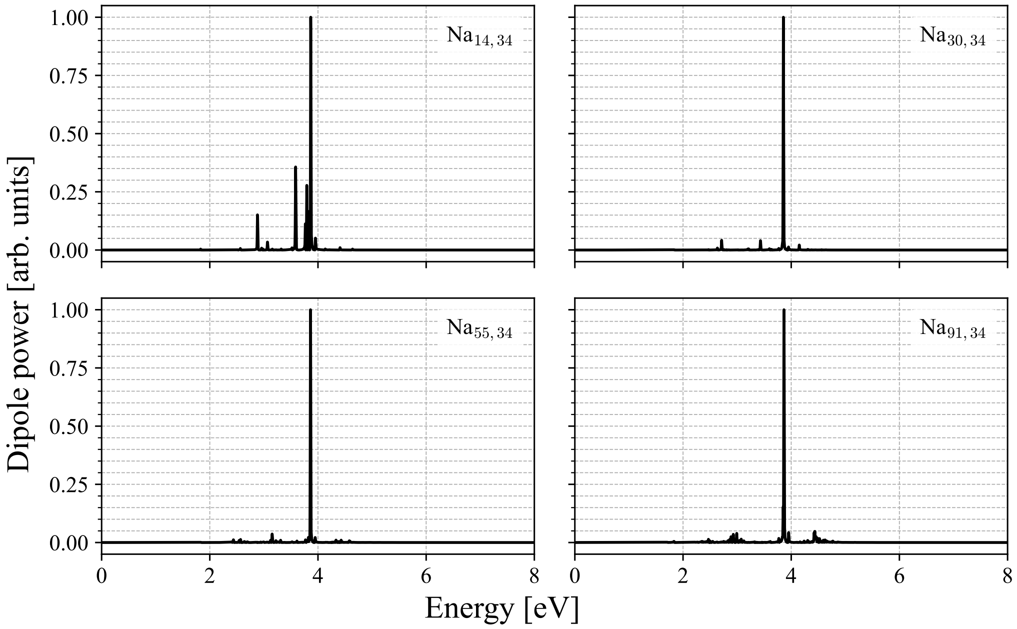

Figure 4.4: Normalized dipole power spectra of the tip-substrate clusters from Fig. 4.3. Confinement-induced shifts with tip growth, while the dominant 3.8 eV peak remains fixed.

To confirm the assignment above, we now vary the substrate sizes with a fixed tip size (Fig. 4.5). The panel (b) in Fig. 4.5 corresponds to the same cluster as panel (a) of Fig. 4.3. Again, to vary the substrate size, we add or remove another atomic layer from the substrate, while the gap of 10 Å remains. The corresponding spectra, as shown in Fig. 4.6, shift and reweight significantly. The previous dominant peak is strongly suppressed or disappears, which further supports the earlier conclusion that the 3.8 eV resonance is, in fact, substrate-dominated.

The observed changes are physically plausible and consistent with quantum confinement. However, a clear trend, such as a uniform spectral blueshift or redshift, is not apparent from the spectra below. This is possibly because multiple modes hybridize and although we vary the cluster size controllably, each modification changes multiple geometric properties

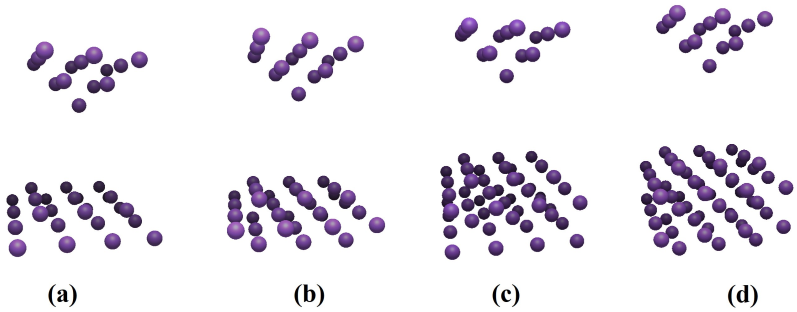

Figure 4.5: Tip-substrate clusters with increasing substrate size at 10 Å gap separation: (a) $Na_{14,25}$; (b) $Na_{14,34}$; (c) $Na_{14,50}$; (d) $Na_{14,59}$.

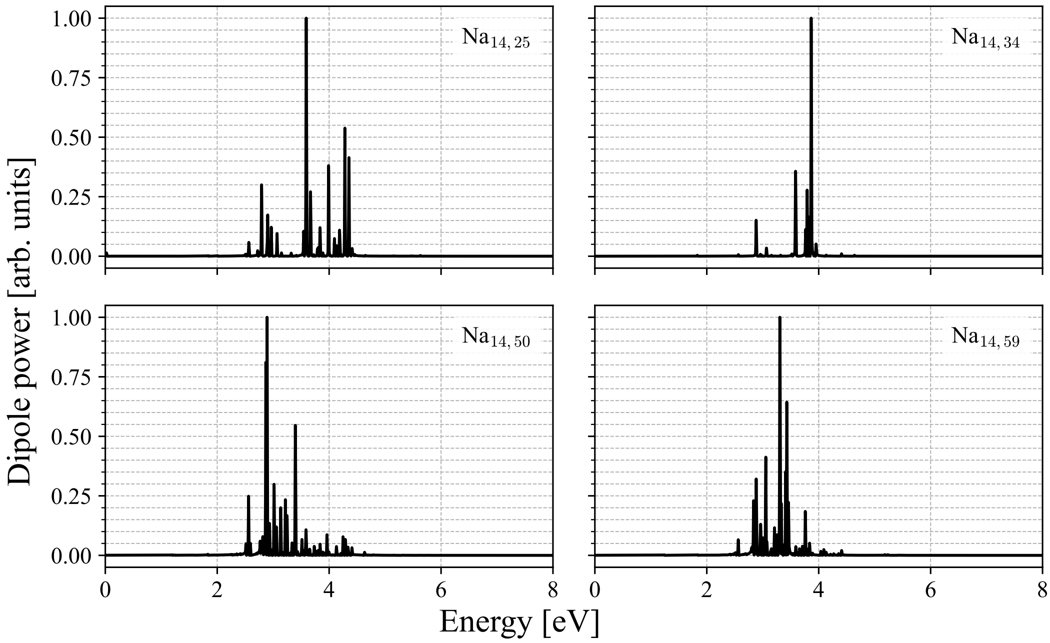

Figure 4.6: Normalized dipole power spectra of the tip-substrate clusters from Fig. 4.5.

(such as apex radius, surface-to-volume ratio, edge/vertex count, etc.) simultaneously. A more systematic investigation, such as varying vertical and lateral dimensions independently and using different geometric shapes, is required to formally establish clear, traceable shift tendencies.

The clusters considered in this work are tiny compared to sizes in real experimental setups, which means the quantitative values of these spectra cannot be extended to macroscopic systems. An open question is whether and beyond which cluster size the confinement effect becomes indistinct. Some studies [25, 26] suggest sizes above which the confinement effect becomes less prominent. In a quick test with our largest system $Na_{140,290}$, we observe a net blueshift of the spectrum compared to smaller clusters from before. This result is consistent with the reported trends for sodium clusters in [27] and hints toward a possible course for the future size-convergence tests (Fig. 4.7). Further dedicated and systematic investigations are needed for reliable quantitative estimates of excitation energies in such systems.

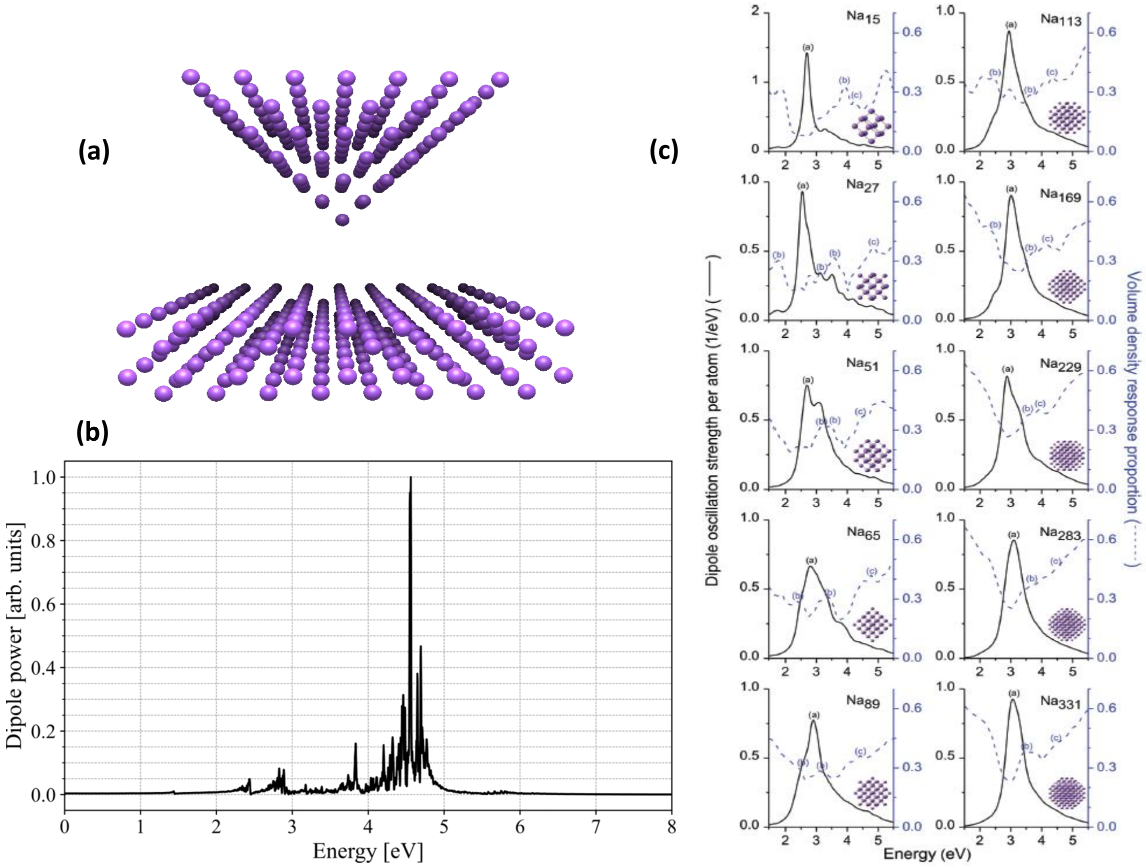

Figure 4.7: (a) $Na_{140,290}$ cluster; (b) normalized dipole power spectrum of $Na_{140,290}$; (c) size-dependent absorption spectra (dipole oscillation strength) of the Na clusters. Here, the volume density response proportion (VRP) spectra are also plotted. Adapted from [27]

4.4 Excitation spectra as a function of tip–substrate distance

In STM-like techniques, tunnel effect is exploited to examine the underlying substrate. It would therefore be very desirable to identify the so-called gap modes in our spectra, which are associated with charge oscillations across the junction from tip to substrate and vice versa. Unfortunately, such modes are not evident from the spectra so far. To enhance their visibility, we systematically vary the tip-substrate separation distance from 14 Å to 3 Å, which is essentially the atomic distance. Such small distances are also accessible in the experimental setups, as demonstrated in [1]. By entering these small gap distances, we expect a significant increase in tunneling probability (Fig. 4.8) and associated changes in the excitation spectra.

For these purposes, we consider three clusters with the same substrate geometries and increasing tip size (Fig. 4.9) and perform distance sweeps between 14 Å and 3 Å. The corresponding distance series are shown in Fig. 4.10 for $Na_{14,34}$, in Fig. B.5 and B.6 for $Na_{30,34}$ and $Na_{55,34}$ clusters, respectively.

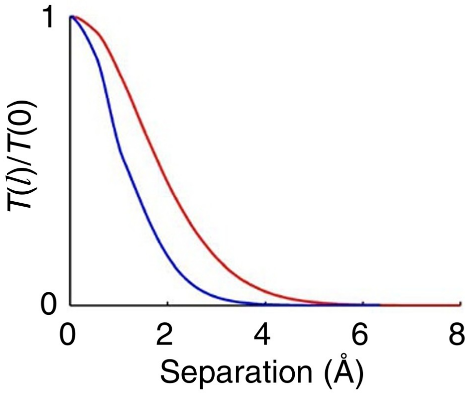

Figure 4.8: Normalized electron tunneling transmission $T(l)/T(0)$ of a plasmonic system composed of two parts, separated by a distanc l and characterized by tunneling transmission $T(l)$. Red corresponds to Na jellium material and blue to Au jellium. Adapted from [28].

To guide the reader, we first walk through the spectra from large to small gaps: At large distances (14–10 Å) the dominant peak remains essentially unchanged. With the gap narrowing from 10 Å to 7 Å and hybridization between the tip and the substrate strengthening, additional features appear and the spectrum exhibits a slight redshift. Below about 7 Å, new low-energy components emerge in the 0-1 eV range, which become more pronounced upon approaching the near-atomic distances. Also noticeable is the gradual blueshift of the overall spectrum in these distances. The same qualitative behavior is also observed for $Na_{30,34}$ and $Na_{55,34}$ clusters (Fig. B.5 and B.6).

We first try to clarify the emergence of the low-energy components at small gaps across all examined clusters. Considering the fact that the tunneling transmission $T(l)$ between two metallic parts should increase as the gap narrows, the first intuitive guess is that these newly appearing features at small separation are tied to the junction itself and the exhibited spectral shifts should also correspond to the behavior of similar metallic setups.

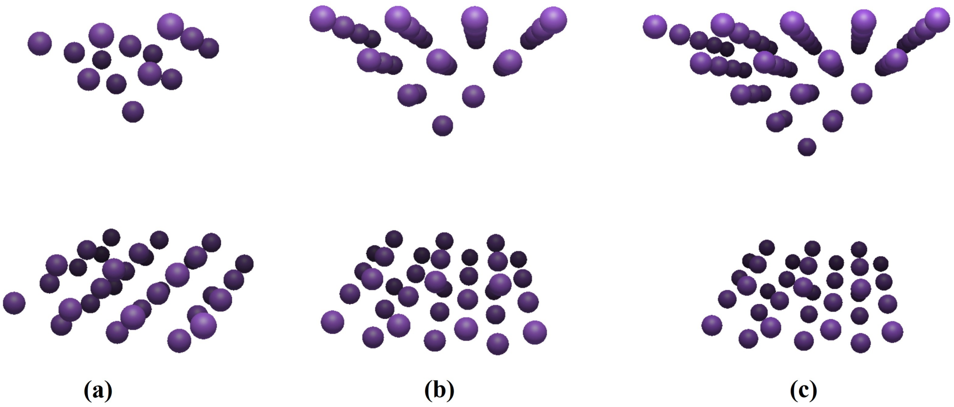

Figure 4.9: Tip–substrate clusters with identical substrates and increasing tip size: (a) $Na_{14,34}$; (b) $Na_{30,34}$; (c) $Na_{55,34}$.

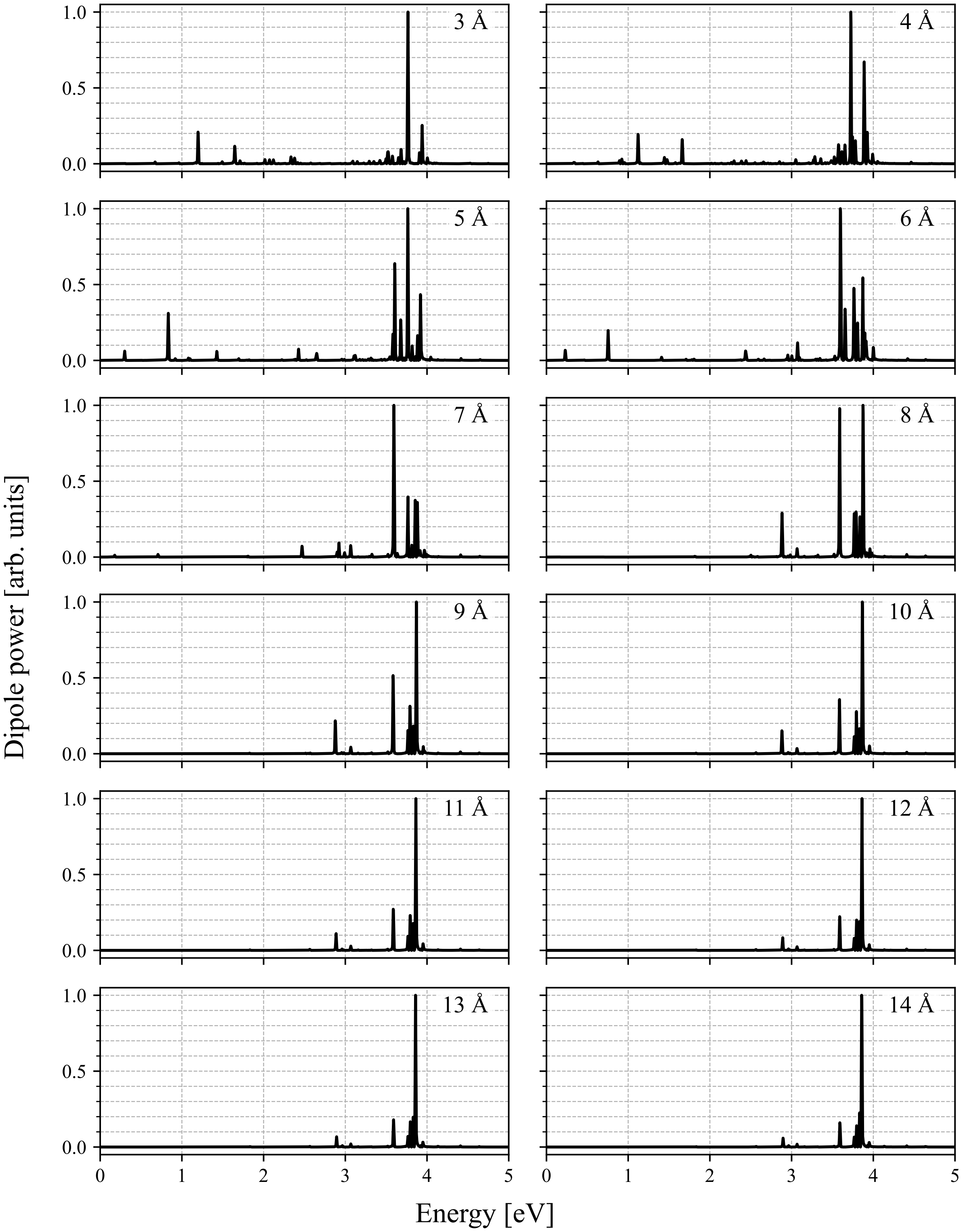

Figure 4.10: Normalized dipole power spectra of $Na_{14,34}$ for gaps of 3 Å to 14 Å.

Therefore, we first compare the spectra of the isolated tips (Na_{14}, Na_{30} and Na_{55}) and the substrate (Na_{34}) used. The spectra of the isolated parts in Fig. 4.11 show the expected confinement trends with increasing tip size and the prominent 3.8 eV peak from the previous section appears in the spectrum of the substrate, confirming its assignment to the substrate.

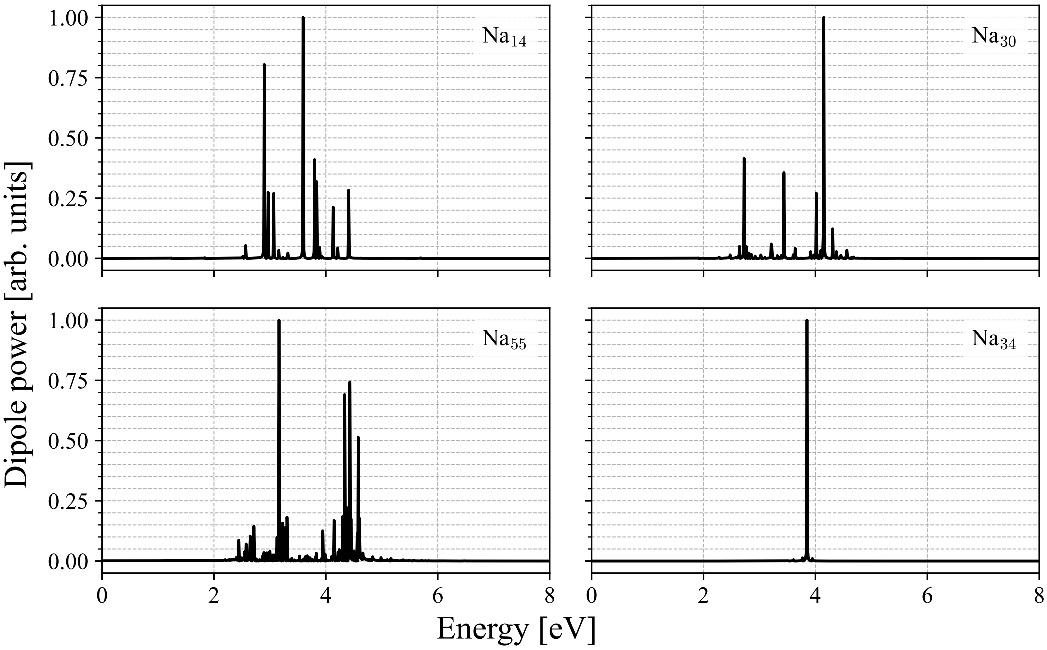

Figure 4.11: Reference spectra of the isolated cluster components: tips Na$_{14}$, Na$_{30}$, Na$_{55}$ and substrate Na$_{34}$.

Importantly, the isolated components do not exhibit the low-energy features that arise at small separations in the coupled systems. This supports the interpretation that the low-energy components are junction-induced modes associated with charge transfer across the gap.

The evolution of the spectra with decreasing distance is consistent with the established metallic dimer model, which distinguishes three interaction regimes: non-contact, tunneling, and contact regimes (Fig. 4.12). The differences in the numerical thresholds for the gap compared to the reference study [28] are due to our geometry, but the qualitative behavior is in very good agreement with the following description:

- Non-contact regime (>7 Å): No significant electron transmission occurs between the tip and the substrate. As the gap narrows, capacitive coupling increases. Consequently, the spectrum slightly redshifts and the near-field is enhanced.

- Tunneling regime (5-7Å): Junction-induced, low-energy modes become more pronounced.

- Contact regime (≤5 Å): When the clusters approach atomic distances, a conductive neck forms and gap modes evolve to charge transfer modes (CTPs). The spectrum gradually blueshifts, including the low-energy components.

By driving our systems into the small-gap regime, we activated the tunneling and can distinguish junction-driven features from other plasmonic resonances localized in the tip or the substrate.

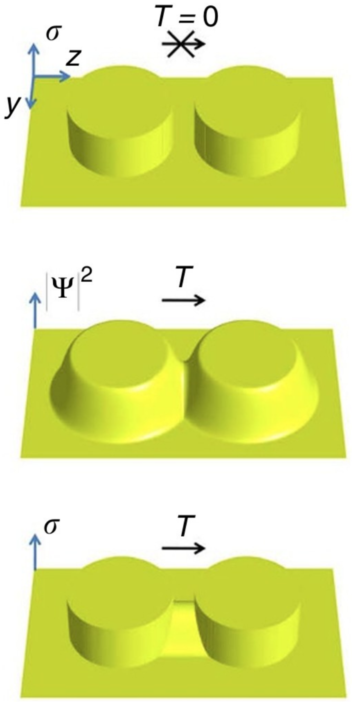

Figure 4.12: Three distinct interaction regimes illustrated by the example of a metallic dimer: non-contact (no electron transfer, $T = 0$), tunneling ($T > 0$) and contact (conductive neck). Adapted from [28].

This provides a way to estimate the tunneling charge density in the gap. For a given excitation energy Ω_n, we can extract the frequency-specific density response and by comparing it to the ground state density the mode-specific induced density can be acquired [4] via

$$\Delta n^{(n)}(\mathbf{r}) \;\approx\; n(\mathbf{r}, \Omega_n) - n_0(\mathbf{r}). \tag{4.2}$$

A tailored algorithmic setup and systematic validation for extracting $\Delta n^{(n)}(\mathbf{r})$ are deferred to future studies. Other potential directions of future works also include quantitative mapping of the three interaction regimes across different shapes and sizes, as well as polarization-resolved $(x/y/z)$ distance sweeps to examine whether the low-energy band is uniquely z-active.

Chapter 5

Conclusion and Outlook

This research set out to determine the excitation spectra of metallic tip-substrate nanostructures using TDDFT calculations and to take first steps toward identifying the modes that reside in the gap. After building the theoretical foundations up to TDDFT and defining how the excitation energies are computed from the time-dependent density, a workflow was established that produces consistent spectral responses within a justified parameter set. Starting from a small tip-substrate model, we tracked the spectral shifts under systematic variations of tip and substrate size. This enabled us to assign selected features to either component of the model and qualitatively observe how confinement affects their positions. Motivated by the pursuit of gap-specific modes, we then performed distance sweeps from atomic distances to $> 1\,\mathrm{nm}$ and successfully isolated features that emerge in small tip-substrate separations across different clusters. The overall junction-induced spectral behavior turned out to be consistent with the well-studied field of plasmonics.

Isolating individual excitation energies opens up the possibility to quantify the charge density that is being transferred across the gap via (4.2) and the associated emitted power via (3.21) with dedicated computational implementations.

Furthermore, in order to provide excitation energies with experimental level accuracy, much larger clusters containing hundreds of thousands of atoms would normally be required for exact representation, significantly increasing the computational costs. However, supported by the literature, we confidently believe there is a numerical threshold above which the spectrum would converge. The search for this threshold should go hand in hand with systematic geometric studies, such as varying vertical and lateral dimensions controllably in tip and substrate, disentangling the contributions of size and shape, etc.

As a final remark, these results clarify the way toward eventually simulating NOTE microscopy with nearly all of its crucial components: exact excitation energies for specific geometries, tunneling charge density and emission power, similar to simulations already existing for other microscopy techniques.

Appendix A

CP2K Code

This Appendix presents the TDDFT input file for CP2K that was used throughout this work.

Code block A.1: CP2K input file for dipole moments following a delta pulse

```
&FORCE_EVAL
  METHOD QUICKSTEP
  &DFT
    BASIS_SET_FILE_NAME  BASIS_MOLOPT_UZH
    POTENTIAL_FILE_NAME  POTENTIAL_UZH
    &MGRID
      CUTOFF 100
    &END MGRID
    &QS
      EPS_DEFAULT 1.0E-10
    &END QS
    &SCF
      SCF_GUESS RESTART
      EPS_SCF 1.0E-7
      MAX_SCF 500
      ADDED_MOS -1
      CHOLESKY INVERSE
      &SMEAR ON
         METHOD FERMI_DIRAC
         ELECTRONIC_TEMPERATURE [K] 300
      &END SMEAR
      &DIAGONALIZATION
         ALGORITHM STANDARD
      &END DIAGONALIZATION
      &MIXING
         METHOD BROYDEN_MIXING
         ALPHA 0.1
         BETA 1.5
         NBROYDEN 8
      &END
    &END SCF
    &POISSON
      PERIODIC NONE
      POISSON_SOLVER MT
    &END POISSON
    &XC
      &XC_FUNCTIONAL PBE
      &END XC_FUNCTIONAL
```

```
    &END XC
    &REAL_TIME_PROPAGATION
      EPS_ITER 1.0E-8 ! Check convergence
      PERIODIC .FALSE.
      MAX_ITER 30
      MAT_EXP ARNOLDI
      EXP_ACCURACY 1.0E-14 ! Less than EPS_ITER
!      INITIAL_WFN RT_RESTART
      APPLY_DELTA_PULSE
      DELTA_PULSE_DIRECTION 0 0 1
      DELTA_PULSE_SCALE 0.001 ! in a.u. of E-field
    &END REAL_TIME_PROPAGATION
    &PRINT
      &MOMENTS
          FILENAME MOMENTS
          PERIODIC FALSE
      &END MOMENTS
    &END PRINT
  &END DFT
  &SUBSYS
    &CELL
      ABC 33 33 55
      PERIODIC NONE
    &END CELL
    &TOPOLOGY
      &CENTER_COORDINATES
      &END CENTER_COORDINATES
      COORD_FILE_NAME   struc.xyz
      COORD_FILE_FORMAT XYZ
    &END TOPOLOGY
    &KIND Na
      BASIS_SET ORB    DZVP-MOLOPT-PBE-GTH-q1
      POTENTIAL        GTH-PBE-q1
    &END KIND
  &END SUBSYS
&END FORCE_EVAL
&GLOBAL
  PROJECT        Propagation_metal_cluster
  RUN_TYPE       RT_PROPAGATION
  EXTENDED_FFT_LENGTHS
&END GLOBAL
&MOTION
    &MD
      ENSEMBLE NVE
      STEPS 25000
      TIMESTEP  0.02 ! timestep in femtoseconds
      TEMPERATURE 300.0
    &END MD
    &PRINT
       &TRAJECTORY
          &EACH
             MD 1
          &END
       &END
    &END
&END MOTION
```

To apply a Gaussian laser pulse, the keywords `APPLY_DELTA_PULSE`, `DELTA_PULSE_DIRECTION`, `DELTA_PULSE_SCALE` must be removed and the following section should be added after `&END XC`:

Code block A.2: Optional Gaussian pulse

```
&EFIELD
  INTENSITY 4.8e8
  WAVELENGTH [nm] 430.0      ! 2.88 eV
  PHASE 0.0
  POLARISATION 1 0 0         ! x-direction
  ENVELOP GAUSSIAN
  &GAUSSIAN_ENV
    SIGMA [fs] 10.6          ! FWHM Full width at half maximum
    T0 [fs] 30.0             ! Pulse maximum at 30 fs
  &END GAUSSIAN_ENV
&END EFIELD
```

The metal cluster is provided in **.xyz** format and the execution is handled by a dedicated run script. Functionalities of all keywords can be found in the official CP2K manual [29].

Appendix B

Additional Data

This appendix presents additional material that support the results discussed in the main part. It includes linearity checks, convergence tests and supplementary spectra.

B.1 Linearity of the dipole responses

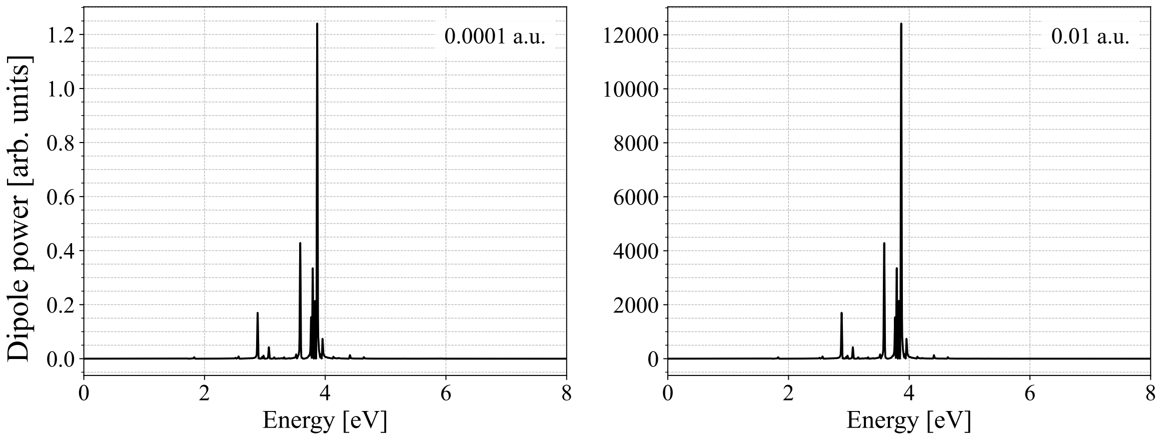

Figure B.1: Dipole power spectrum of the $Na_{14,34}$ cluster, excited by delta pulses with strengths of 0.0001 a.u. (left) and 0.01 a.u. (right). The dipole power scales quadratically with the impulse strength and importantly, no other spectral differences are observed between the two spectra.

B.2 Convergence tests

The convergence tests demonstrate that the total propagation time of 500 fs is sufficient for the peak positions and their relative amplitudes to stabilize, as seen from the spectral evolution with increasing simulation length (Figures B.2, B.3, B.4).

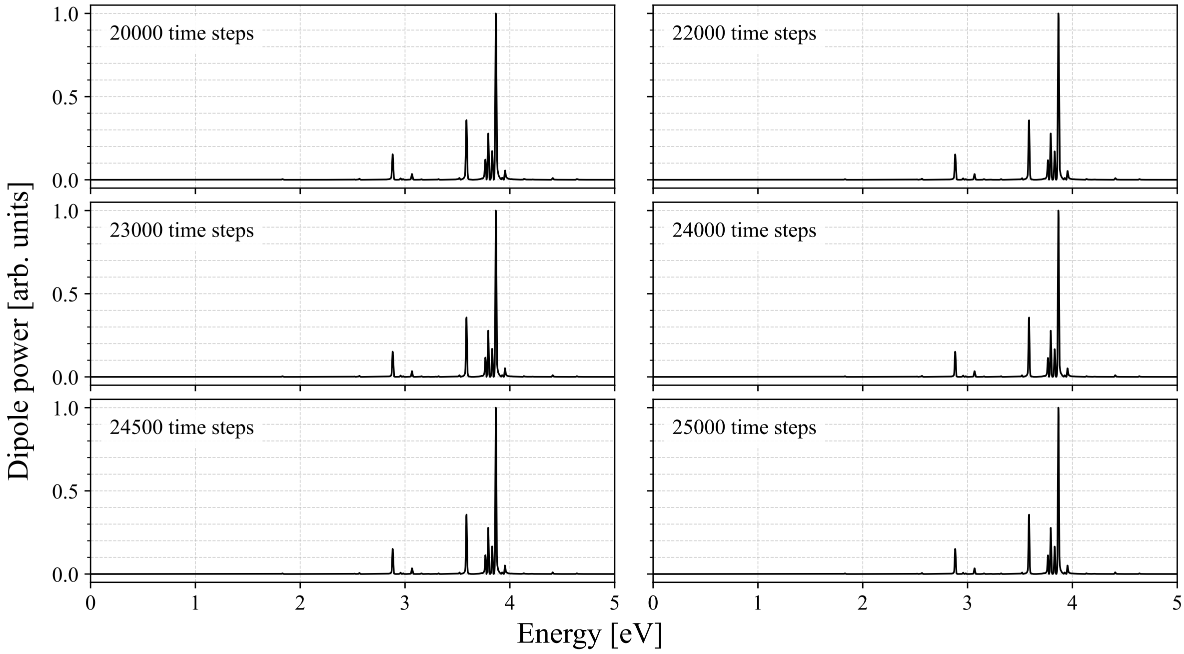

Figure B.2: Time-convergence of the dipole power spectra for the $\mathrm{Na}_{14,34}$ tip-substrate system (20000–25000 steps, $\Delta t = 0.02\,\mathrm{fs}$).

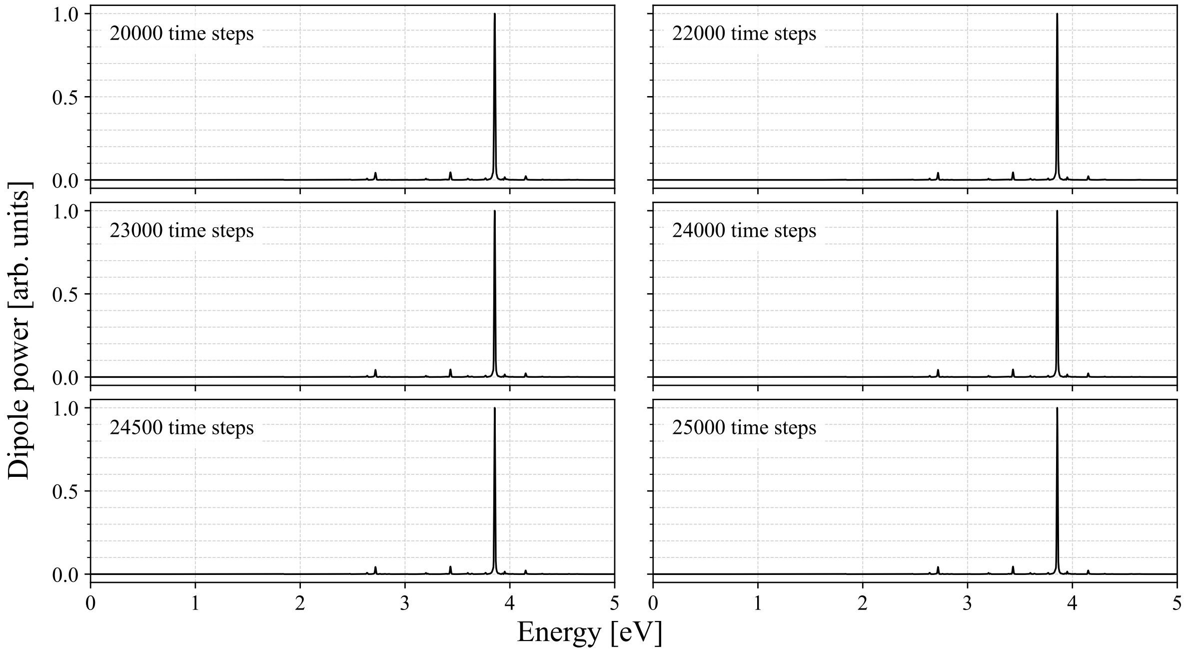

Figure B.3: Time-convergence of the dipole power spectra for the $\mathrm{Na}_{30,34}$ tip-substrate system (20000–25000 steps, $\Delta t = 0.02\,\mathrm{fs}$).

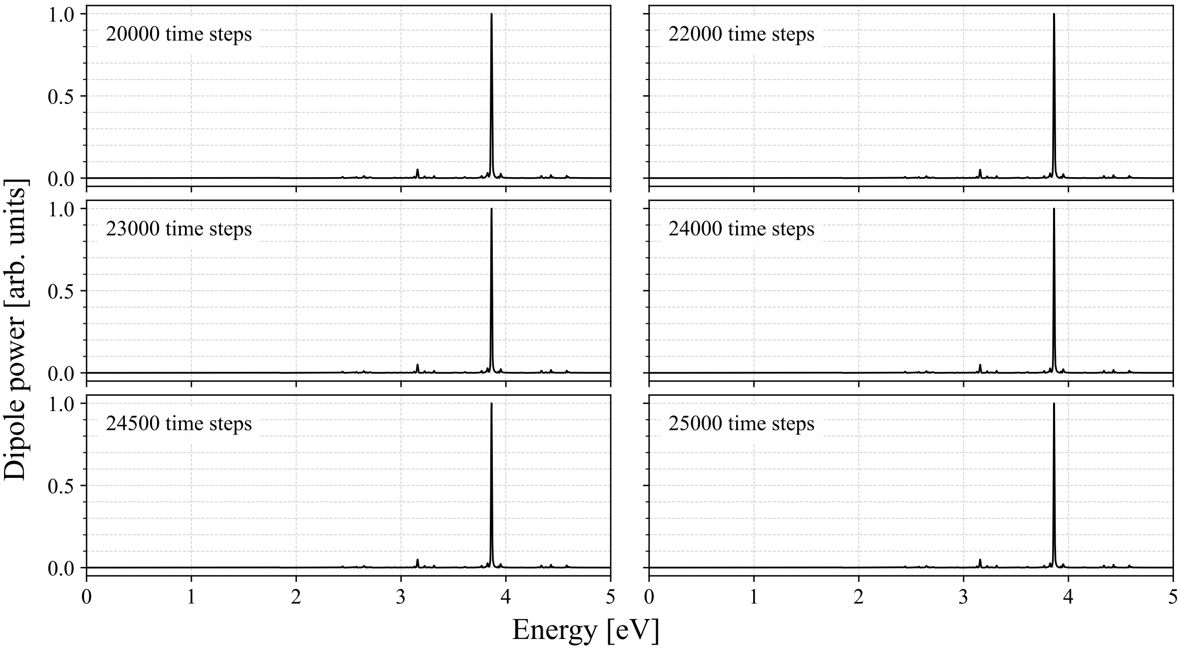

Figure B.4: Time-convergence of the dipole power spectra for the $\mathrm{Na}_{55,34}$ tip-substrate system (20000–25000 steps, $\Delta t = 0.02\,\mathrm{fs}$).

B.3 Distance tests

The distance-dependent spectra (3 Å to 14 Å) of $Na_{30,34}$ and $Na_{55,34}$ clusters are shown below.

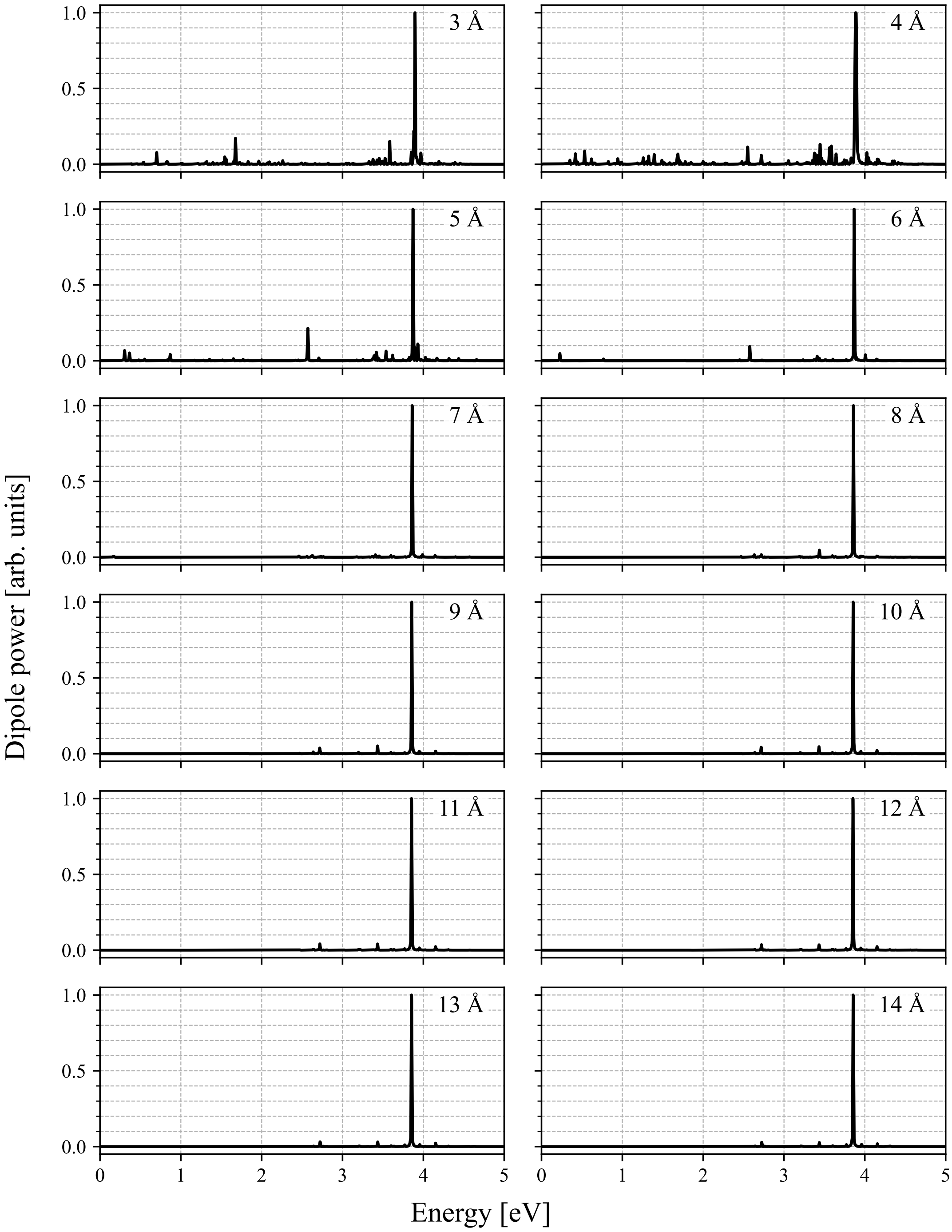

Figure B.5: Normalized dipole power spectra of $Na_{30,34}$ for gaps of 3 Å to 14 Å.

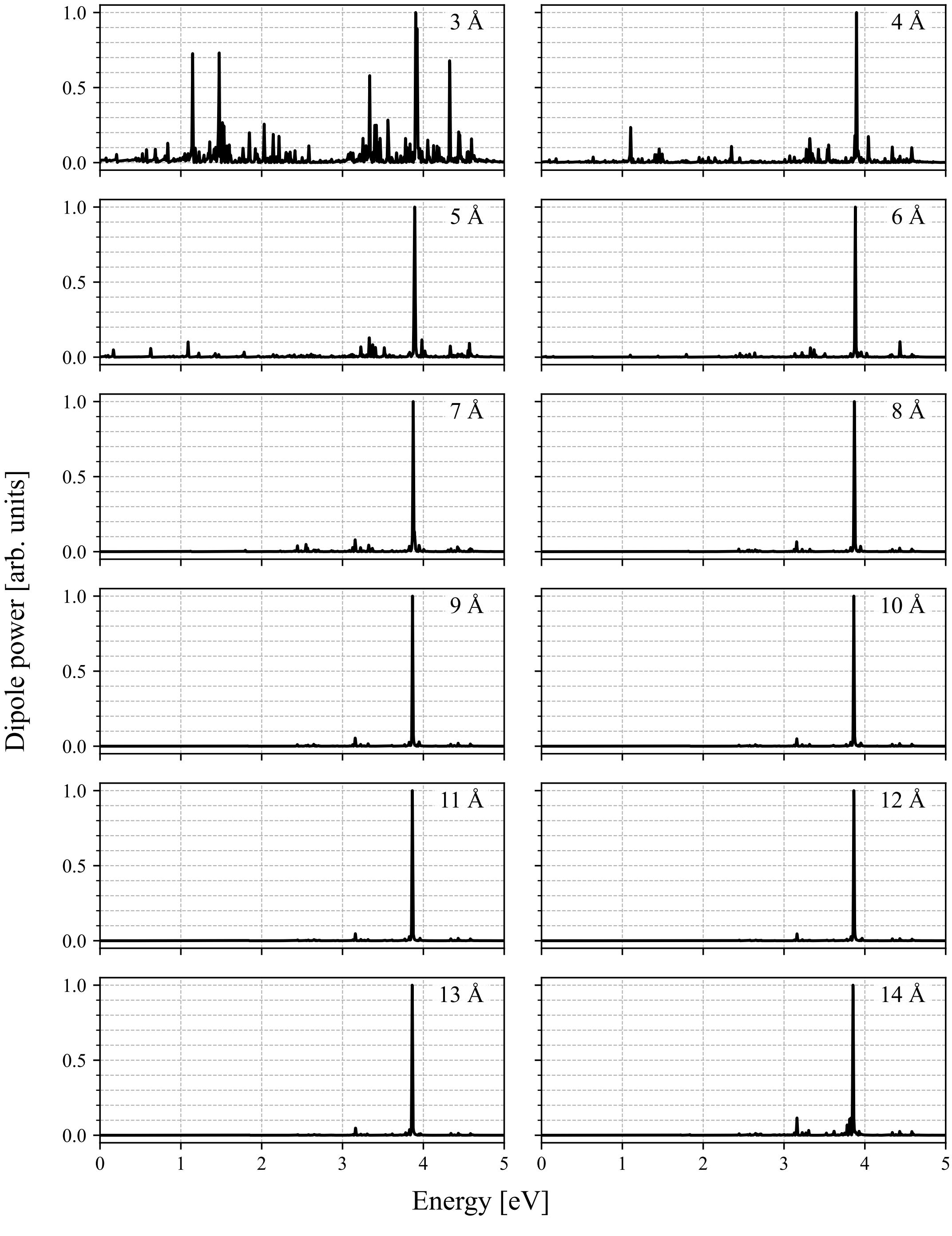

Figure B.6: Normalized dipole power spectra of $Na_{55,34}$ for gaps of 3 Å to 14 Å.

Bibliography

[1] T. Siday, J. Hayes, F. Schiegl, F. Sandner, P. Menden, V. Bergbauer, M. Zizlsperger, S. Nerreter, S. Lingl, J. Repp, J. Wilhelm, M. A. Huber, Y. A. Gerasimenko, and R. Huber, *All-optical subcycle microscopy on atomic length scales*, Nature **629**, 329–334 (2024).

[2] J. Wilhelm. *Computational Nanoscience: Lecture Notes*. University of Regensburg. 2024.

[3] F. Calvayrac, P. Reinhard, and E. Suraud, *Spectral Signals from Electronic Dynamics in Sodium Clusters*, Annals of Physics **255**, 125–162 (1997).

[4] C. A. Ullrich, *Time-Dependent Density-Functional Theory: Concepts and Applications*, Oxford University Press, 2012.

[5] R. G. Parr and W. Yang, *Density-Functional Theory of Atoms and Molecules*, Oxford University Press, 1989.

[6] F. Jensen, *Introduction to Computational Chemistry*, Wiley, 1999.

[7] W. Koch and M. C. Holthausen, "The Hohenberg–Kohn Theorems", in *A Chemist's Guide to Density Functional Theory*. Wiley-VCH (2001).

[8] P. Hohenberg and W. Kohn, *Inhomogeneous Electron Gas*, Phys. Rev. **136**, B864–B871 (1964).

[9] R. Martin, *Electronic Structure: Basic Theory and Practical Methods*, , 2020.

[10] J. F. Janak, *Proof that $\frac{\partial E}{\partial n_i} = \epsilon$ in density-functional theory*, Phys. Rev. B **18**, 7165–7168 (1978).

[11] J. VandeVondele and J. Hutter, *Gaussian basis sets for accurate calculations on molecular systems in gas and condensed phases*, The Journal of Chemical Physics **127**, 114105 (2007).

[12] S. Goedecker, M. Teter, and J. Hutter, *Separable dual-space Gaussian pseudopotentials*, Phys. Rev. B **54**, 1703–1710 (1996).

[13] D. R. Hamann, M. Schlüter, and C. Chiang, *Norm-Conserving Pseudopotentials*, Phys. Rev. Lett. **43**, 1494–1497 (1979).

[14] A. D. Becke, *Density-functional exchange-energy approximation with correct asymptotic behavior*, Phys. Rev. A **38**, 3098–3100 (1988).

[15] J. P. Perdew, K. Burke, and M. Ernzerhof, *Generalized Gradient Approximation Made Simple*, Phys. Rev. Lett. **77**, 3865–3868 (1996).

[16] J. P. Perdew and K. Schmidt, *Jacob's ladder of density functional approximations for the exchange-correlation energy*, AIP Conference Proceedings **577**, 1–20 (2001).

[17] E. Runge and E. K. U. Gross, *Density-Functional Theory for Time-Dependent Systems*, Phys. Rev. Lett. **52**, 997–1000 (1984).

[18] R. van Leeuwen, *Mapping from Densities to Potentials in Time-Dependent Density-Functional Theory*, Phys. Rev. Lett. **82**, 3863–3866 (1999).

[19] M. D. Hanwell, D. E. Curtis, D. C. Lonie, T. Vandermeersch, E. Zurek, and G. R. Hutchison, *Avogadro: an advanced semantic chemical editor, visualization, and analysis platform*, Journal of Cheminformatics **4**, 17 (2012).

[20] J. D. Jackson, *Classical Electrodynamics*, Wiley, 2nd edition, 1975.

[21] W. Parson and C. Burda, *Modern Optical Spectroscopy: From Fundamentals to Applications in Chemistry, Biochemistry and Biophysics*, Springer International Publishing, 2023.

[22] M. Khan, K. Majeed, and M. A. Shar, *Metals Doped CdS Quantum Dots: Structural, Optical and Photocatalytic Properties under Visible Light Irradiation*, International Journal of Metallurgy and Metal Physics **5**, (2020).

[23] Peller, Roelcke, Kastner, Buchner, Neef, Hayes, Bonafé, Sidler, Ruggenthaler, Rubio, Huber, and Repp, *Quantitative sampling of atomic-scale electromagnetic waveforms*, Nature Photonics **15**, 143–147 (2021).

[24] M. Dalal, *A Textbook of Physical Chemistry – Volume 1*, Dalal Institute, 2018.

[25] N. J. Halas, S. Lal, W.-S. Chang, S. Link, and P. Nordlander, *Plasmons in strongly coupled metallic nanostructures*, Chemical reviews **111**, 3913–3961 (2011).

[26] S. Lu, L. Xie, K. Lai, R. Chen, L. Cao, K. Hu, X. Wang, J. Han, X. Wan, J. Wan, Q. Dai, F. Song, J. He, J. Dai, J. Chen, Z. Wang, and G. Wang, *Plasmonic evolution of atomically size-selected Au clusters by electron energy loss spectrum*, National Science Review **8**, nwaa282 (2020).

[27] J.-H. Li, M. Hayashi, and G.-Y. Guo, *Plasmonic excitations in quantum-sized sodium nanoparticles studied by time-dependent density functional calculations*, Phys. Rev. B **88**, 155437 (2013).

[28] R. Esteban, A. G. Borisov, P. J. Nordlander, and J. Aizpurua, *Bridging quantum and classical plasmonics with a quantum-corrected model*, Nature Communications **3**, (2012).

[29] CP2K Developers. *CP2K Manual.* Accessed: 01/09/2025. 2025. URL: `https://manual.cp2k.org/`.

Acknowledgments

I would like to thank my supervisor Dr. Jan Wilhelm for always taking the time to guide me through this research and for his continuous support. Special thanks go to Dr. Štěpán Marek for sharing his expertise and helping me overcome computational challenges. I am also grateful to Furkan Özyiğit from the Chair of Quantum Nanoscience for brainstorming ideas with me and for his encouragement. Finally, I thank the members of Prof. Dr. Evers's chair and Prof. Dr. Evers personally for the warm welcome and support.

Declaration of Authorship

Hiermit versichere ich, dass ich die vorliegende Arbeit selbstständig verfasst und keine anderen Hilfsmittel als die angegebenen verwendet habe. Die Stellen, die anderen Werken (gilt ebenso für Werke aus elektronischen Datenbanken oder aus dem Internet) wörtlich oder sinngemäß entnommen sind, habe ich unter Angabe der Quelle und Einhaltung der Regeln wissenschaftlichen Zitierens kenntlich gemacht. Über wissenschaftlich korrektes Arbeiten wurde ich aufgeklärt. Diese Versicherung umfasst auch in der Arbeit verwendete bildliche Darstellungen, Tabellen, Kartenskizzen und gelieferte Zeichnungen. Ebenso versichere ich, dass die vorgelegten Druckexemplare und die abgegebene elektronische Version der Arbeit identisch sind, sowie, dass ich diese Arbeit nicht bereits an einer anderen Universität zur Erlangung eines akademischen Grades eingereicht habe. Mir ist bewusst, dass Täuschungen nach der für mich gültigen Studien- und Prüfungsordnung geahndet werden. Ich habe Kenntnis von den in § 26 Abs. 5 vorgesehenen Rechtsfolgen.

Unterschrift	Ort, Datum